Finite bending and pattern evolution of the associated instability for a dielectric elastomer slab

Yipin Su [a,b], Bin Wu [a], Weiqiu Chen [a], Michel Destrade [a,b,*]

[a] Department of Engineering Mechanics, Zhejiang University, Hangzhou 310027, PR China
[b] School of Mathematics, Statistics and Applied Mathematics, NUI Galway, University Road, Galway, Ireland

ABSTRACT

We investigate the finite bending and the associated bending instability of an incompressible dielectric slab subject to a combination of applied voltage and axial compression, using nonlinear electro-elasticity theory and its incremental version. We first study the static finite bending deformation of the slab. We then derive the three-dimensional equations for the onset of small-amplitude wrinkles superimposed upon the finite bending. We use the surface impedance matrix method to build a robust numerical procedure for solving the resulting dispersion equations and determining the wrinkled shape of the slab at the onset of buckling. Our analysis is valid for dielectrics modeled by a general free energy function. We then present illustrative numerical calculations for ideal neo-Hookean dielectrics. In that case, we provide an explicit treatment of the boundary value problem of the finite bending and derive closed-form expressions for the stresses and electric field in the body. For the incremental deformations, we validate our analysis by recovering existing results in more specialized contexts. We show that the applied voltage has a destabilizing effect on the bending instability of the slab, while the effect of the axial load is more complex: when the voltage is applied, changing the axial loading will influence the true electric field in the body, and induce competitive effects between the circumferential instability due to the voltage and the axial instability due to the axial compression. We even find circumstances where both instabilities cohabit to create two-dimensional patterns on the inner face of the bent sector.

© 2018 Elsevier Ltd. All rights reserved.

1. Introduction

An elastic rectangular slab can be bent into a cylindrical sector under the application of moments on the lateral faces, and the bending angle depends on the applied moments, the dimensions and the material properties of the slab. The finite bending deformation of incompressible soft materials is well captured by the theory of nonlinear elasticity (Rivlin, 1949; Green and Zerna, 1954; Truesdell and Toupin, 1960; Ogden, 1997). Generally speaking, the inner surface of a bent slab is contracted circumferentially, and the outer surface is stretched. Experimental observations indicate that wrinkles and creases will appear on the compressed surface of a bent rubber slab if the circumferential stretch of the inner surface reaches a critical value, i.e., the so-called bending instability occurs (Gent and Cho, 1999). This phenomenon can be predicted by the theory of incremental nonlinear elasticity (Triantafyllidis, 1980; Destrade et al., 2009a,b, 2014; Roccabianca et al., 2010).

Dielectric elastomers are novel smart materials with the ability to convert mechanical energy into electrical energy, and vice versa. Dielectric elastomers have attracted considerable attention from academia and industry alike because, compared with other smart materials like electroactive ceramics and shape memory alloys, they have the advantages of fast response, high-sensitivity, low noise and large actuation strain, making them ideal candidates to develop high-performance devices such as actuators, soft robots, artificial muscles, phononic devices and energy harvesters (Bar-Cohen, 2004; Kim and Tadokoro, 2007; Rasmussen, 2012; Brochu and Pei, 2010; Galich and Rudykh, 2017; Getz and Shmuel, 2017; Wu et al., 2018). Generally, a dielectric actuator is composed of a soft elastomeric material sandwiched between two compliant electrodes (typically, by brushing on carbon grease). Application of a voltage across the thickness of the actuator generates electrostatic forces, which lead to a reduction in the thickness and an expansion in the area of the actuator. Based on this mechanism, various dielectric devices have been designed to achieve giant actuation strains (Pelrine et al., 2000; O'Halloran et al., 2008; Zhang et al., 2017).

* Corresponding author at: School of Mathematics, Statistics and Applied Mathematics, NUI Galway, University Road, Galway, Ireland.
  E-mail address: michel.destrade@nuigalway.ie (M. Destrade).
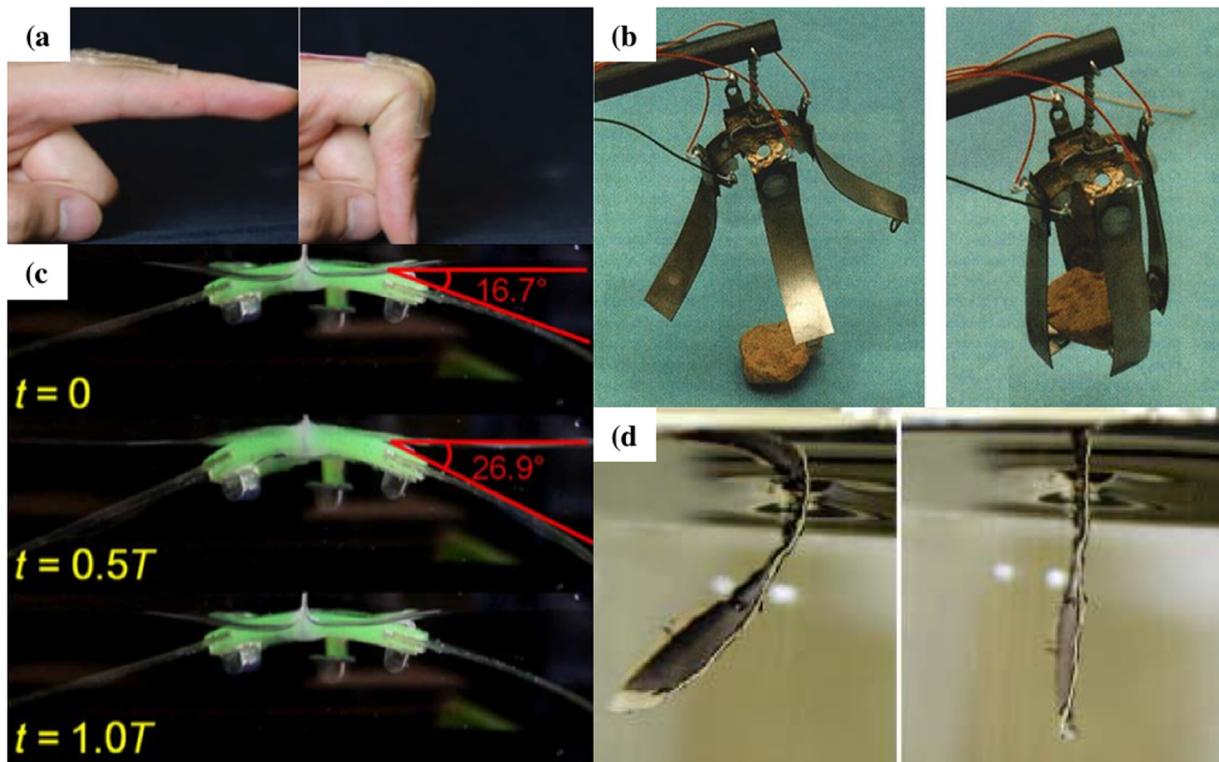
Fig. 1. Bending deformations in dielectric devices: (a) A strain sensor consisting of a stretchable dielectric sandwiched between two flexible ionic conductors attached to a straight finger: the bending of the finger stretches the sensor (Sun et al., 2014); (b) A 4-finger dielectric gripper: this actuator induces voltage-driven bending to lift a rock (Bar-Cohen, 2002); (c) Bending variations of the soft body and fins of a soft electronic "fish" made of dielectric elastomer and ionically conductive hydrogel: the fish can swim at a fast speed driven by periodical bending deformations (Li et al., 2017); (d) A dielectric actuator with a significant voltage-driven bending response (Bar-Cohen, 2002).

To understand the electromechanical coupling effect and predict the nonlinear response of dielectric elastomers subject to electromechanical loadings, a nonlinear field theory is required. Arguably, Toupin (1956) was the first to develop a general nonlinear theory of electro-elasticity. Much effort has been devoted to the development of this theory in the last two decades (Ericksen, 2007; Suo et al., 2008; Liu, 2013; Dorfmann and Ogden, 2016), driven by recent applications in the real-world. So far, several finite deformations of dielectric structures have been investigated theoretically, including simple shear of a dielectric slab (Dorfmann and Ogden, 2005), in-plane homogeneous deformation of a dielectric plate (Dorfmann and Ogden, 2014a), extension and inflation of a dielectric tube (Dorfmann and Ogden, 2006; Zhu et al., 2010) and a multilayer dielectric tube (Bortot, 2018), inflation of a dielectric sphere (Li et al., 2013; Dorfmann and Ogden, 2014b) and of a multilayer dielectric sphere (Bortot, 2017).

Finite bending deformation is common in devices based on dielectric elastomers, see examples in Fig. 1, but little attention has been devoted to the theoretical analysis of this deformation for dielectric structures. Wissman et al. (2014) studied the pure bending of a dielectric elastomer actuator which contains inextensible but flexible frames. They simplified the kinematics by assuming plane strain deformation and modeled the bending deformation using elastic shell theory based on the principle of minimum potential energy. Good agreement between theoretical and experimental results was achieved for a neo-Hookean constitutive law, but the prediction is valid only for small strain deformation. Li et al. (2014) investigated the bending deformation of a dielectric spring-roll. The allowable bending of the actuator was determined by considering several failure models, including electromechanical instability, electrical breakdown, and tensile rupture. There also, the small strain assumption was adopted to simplify the problem. Only recently was a theoretical study on the finite bending of a dielectric ac-

tuator based on the three-dimensional nonlinear electro-elasticity made available (He et al., 2017). There, the authors considered an actuator consisting of a hyperelastic layer and two pre-stretched dielectric elastomer layers, which bends once a voltage is applied through the thickness of the dielectric layer. That analysis was concerned with static finite bending under the plane strain assumption but not with the associated bending instability.

In this paper, we propose a theoretical analysis of finite bending deformation and the associated bending instability of an incompressible dielectric slab subject to the combined action of electrical voltage and mechanical loads. We focus on how finite bending and bending instability of a dielectric slab are influenced by tuning the applied voltage, the structural parameters and the axial compression.

The paper is structured as follows. In Section 2, we briefly recall the general equations of the nonlinear theory of electro-elasticity and the associated linear incremental field theory (Dorfmann and Ogden, 2016). We then specialize the general theory to the problems of the finite bending and the linearized incremental motion superposed upon the bending of a dielectric slab modeled by any form of energy function (Section 3). We arrange the governing incremental equations in the Stroh form and then use the surface impedance matrix method to obtain a robust numerical procedure for deriving the bending and compression thresholds for the onset of the instability. We find the corresponding wrinkled shape of the slab when buckling occurs. In Section 4, we present numerical calculations for an ideal neo-Hookean dielectric slab to elucidate the influence of the applied voltage, of the structural parameters and of the axial compression on the finite bending and the associated buckling behavior. We show analytically that only moments are required to drive the large bending of the slab. We find that both the applied voltage and the axial constraint pose a destabilizing effect on the slab, while these two effects compete with each other

because compressing the slab will decrease the true electric field in the solid. We also find under which circumstances can a two-dimensional buckling pattern happen, where circumferential and axial wrinkles co-exist. Finally in Section 5, we draw some conclusions.

2. Basic formulation

In this section we propose a brief overview of the governing equations for finite electro-elasticity and its associated incremental theory. Interested readers are referred to the textbook by Dorfmann and Ogden (2016) for more detailed background on this topic.

2.1. Finite electro-elasticity

Consider a deformable continuous electrostatic body which, at time t_0, occupies an undeformed, stress-free configuration B_r, with boundary ∂B_r and outward unit normal vector $\mathbf{N}$. Assume that the body is subject to a (true) electric field $\mathbf{E}$, with an associated (true) electric displacement $\mathbf{D}$. A material particle in B_r labeled by its position vector $\mathbf{X}$ takes up the position $\mathbf{x}$ at time t, after a finite deformation described by the mapping $\mathbf{x} = \chi(\mathbf{X}, t)$, where χ is twice continuously differentiable. As a result, the body deforms quasi-statically into the current configuration, which is denoted by B_t, with the boundary ∂B_t and the outward unit normal vector $\mathbf{n}$. The deformation gradient tensor is $\mathbf{F} = \partial \mathbf{x}/\partial \mathbf{X}$, with Cartesian components $F_{i\alpha} = \partial x_i/\partial X_\alpha$. The initial volume element $d\delta$ and the deformed volume element $d\Delta$ of the solid are related by $d\delta = J d\Delta$, where $J = \det \mathbf{F}$ is the local volume ratio.

Throughout this paper we consider incompressible dielectric elastomers, for which the internal constraint $J \equiv 1$ holds at all times. According to the theory of nonlinear electro-elasticity, by introducing an augmented free energy function $\Omega = \Omega(\mathbf{F}, \mathbf{D}_l)$, which is defined in the reference configuration, the governing equations of the body can be obtained as

$$\mathbf{T} = \frac{\partial \Omega}{\partial \mathbf{F}} - p\mathbf{F}^{-1}, \quad \mathbf{E}_l = \frac{\partial \Omega}{\partial \mathbf{D}_l}, \tag{1}$$

where $\mathbf{T} = \mathbf{F}^{-1}\boldsymbol{\tau}$ is the total nominal stress, with $\boldsymbol{\tau}$ being the total Cauchy stress tensor, p is a Lagrange multiplier associated with the incompressibility constraint, which can be determined from the boundary conditions, and the nominal electric field $\mathbf{E}_l = \mathbf{F}^{\mathrm{T}}\mathbf{E}$ and the nominal electric displacement $\mathbf{D}_l = \mathbf{F}^{-1}\mathbf{D}$ are the Lagrangian counterparts of $\mathbf{E}$ and $\mathbf{D}$, respectively. The superscripts '−1' and 'T' throughout this paper denote the inverse and transpose of a tensor, respectively.

Specifically, for an isotropic, incompressible, electro-elastic material, Ω can be expressed in terms of the following five invariants

$$I_1 = \mathrm{tr}\,\mathbf{c}, \quad I_2 = \mathrm{tr}(\mathbf{c}^{-1}), \quad I_4 = \mathbf{D}_l \cdot \mathbf{D}_l,$$
$$I_5 = \mathbf{D}_l \cdot \mathbf{c}\mathbf{D}_l, \quad I_6 = \mathbf{D}_l \cdot \mathbf{c}^2\mathbf{D}_l, \tag{2}$$

where $\mathbf{c} = \mathbf{F}^{\mathrm{T}}\mathbf{F}$ is the right Cauchy-Green deformation tensor. Combined with Eq. (1), the Cauchy stress $\boldsymbol{\tau} = \mathbf{F}\mathbf{T}$ and the electric field $\mathbf{E} = \mathbf{F}^{-\mathrm{T}}\mathbf{E}_l$ are found as

$$\boldsymbol{\tau} = 2\Omega_1\mathbf{b} + 2\Omega_2(I_1\mathbf{b} - \mathbf{b}^2) - p\mathbf{I} + 2\Omega_5\mathbf{D} \otimes \mathbf{D}$$
$$+ 2\Omega_6(\mathbf{D} \otimes \mathbf{b}\mathbf{D} + \mathbf{b}\mathbf{D} \otimes \mathbf{D}), \tag{3}$$

$$\mathbf{E} = 2(\Omega_4\mathbf{b}^{-1}\mathbf{D} + \Omega_5\mathbf{D} + \Omega_6\mathbf{b}\mathbf{D}), \tag{4}$$

where $\mathbf{I}$ is identity tensor, $\mathbf{b} = \mathbf{F}\mathbf{F}^{\mathrm{T}}$ is the left Cauchy-Green deformation tensor and the shorthand notation $\Omega_m = \partial \Omega/\partial I_m (m = 1, 2, 4, 5, 6)$ is adopted here and henceforth.

In the absence of body forces, free charges and currents, and applying the 'quasi-electrostatic approximation', the equations of equilibrium read

$$\mathrm{div}\,\boldsymbol{\tau} = \mathbf{0}, \quad \mathrm{curl}\,\mathbf{E} = \mathbf{0}, \quad \mathrm{div}\,\mathbf{D} = 0, \tag{5}$$

where 'div' and 'curl' are the divergence and curl operators defined in the deformed configuration, respectively.

In this paper, we consider an initially stress-free dielectric slab, with flexible electrodes glued to its upper and bottom surfaces, which is bent into a circular sector by the combined action of electric voltage and mechanical loadings. In this case, the electric field in the body is distributed radially in the deformed configuration and there is no exterior electric field in the surrounding vacuum. Then the fields must satisfy the following boundary conditions on the bent surfaces,

$$\boldsymbol{\tau}\mathbf{n} = \mathbf{t}_a, \quad \mathbf{E} \times \mathbf{n} = \mathbf{0}, \quad \mathbf{D} \cdot \mathbf{n} = q_e, \tag{6}$$

where $\mathbf{t}_a$ is the prescribed mechanical traction per unit area of ∂B_t, and q_e is the surface charge density on ∂B_t.

2.2. Incremental motions

We now superimpose an infinitesimal incremental deformation $\dot{\mathbf{x}}$ along with an infinitesimal increment in the electric displacement $\dot{\mathbf{D}}_l$. Hereinafter, dotted variables represent incremental quantities. The incremental form of the aforementioned equations can be obtained by Taylor expansions. Hence, the linearized incremental forms of the constitutive relations in Eq. (1) read

$$\dot{\mathbf{T}}_0 = \mathbf{A}_0\mathbf{H} + \mathbf{\Gamma}_0\dot{\mathbf{D}}_{l0} + p\mathbf{H} - \dot{p}\mathbf{I}, \quad \dot{\mathbf{E}}_{l0} = \mathbf{\Gamma}_0^T\mathbf{H} + \mathbf{K}_0\dot{\mathbf{D}}_{l0}, \tag{7}$$

where $\dot{\mathbf{T}}_0 = \mathbf{F}\dot{\mathbf{T}}, \dot{\mathbf{E}}_{l0} = \mathbf{F}^{-\mathrm{T}}\dot{\mathbf{E}}_l$ and $\dot{\mathbf{D}}_{l0} = \mathbf{F}\dot{\mathbf{D}}_l$ are the 'push forward' versions of $\dot{\mathbf{T}}, \dot{\mathbf{E}}_l$ and $\dot{\mathbf{D}}_l$, respectively, $\mathbf{H} = \mathrm{grad}\,\mathbf{u}$ is the displacement gradient, with $\mathbf{u}(\mathbf{x}, t) = \dot{\mathbf{x}}(\mathbf{X}, t)$ being the incremental mechanical displacement, and $\mathbf{A}_0$, $\mathbf{\Gamma}_0$ and $\mathbf{K}_0$ are, respectively, fourth-, third- and second-order tensors, with Cartesian components defined by

$$A_{0piqj} = A_{0qjpi} = F_{p\alpha}F_{q\beta}\frac{\partial^2\Omega}{\partial F_{i\alpha}\partial F_{j\beta}}, \quad \Gamma_{0piq} = \Gamma_{0ipq} = F_{p\alpha}F_{\beta q}^{-1}\frac{\partial^2\Omega}{\partial F_{i\alpha}\partial D_{l\beta}},$$

$$K_{0ij} = K_{0ji} = F_{\alpha i}^{-1}F_{\beta j}^{-1}\frac{\partial^2\Omega}{\partial D_{l\alpha}\partial D_{l\beta}}. \tag{8}$$

The above defined tensors are the so-called 'electro-elastic moduli tensors', which are fully determined once the energy function Ω and biasing fields $\mathbf{F}$ and $\mathbf{D}_l$ are prescribed.

It is worth noting here that we have the connection

$$A_{0jilk} - A_{0ijlk} = (\tau_{jl} + p\delta_{jl})\delta_{ik} - (\tau_{il} + p\delta_{il})\delta_{jk}, \tag{9}$$

which can be established by using the incremental form of the symmetry condition of the Cauchy stress $\mathbf{F}\mathbf{T} = (\mathbf{T}\mathbf{F})^{\mathrm{T}}$.

The incremental forms of the equilibrium equations in (5) are

$$\mathrm{div}\,\dot{\mathbf{T}}_0 = \mathbf{0}, \quad \mathrm{curl}\,\dot{\mathbf{E}}_{l0} = \mathbf{0}, \quad \mathrm{div}\,\dot{\mathbf{D}}_{l0} = 0. \tag{10}$$

In addition, the incremental incompressibility constraint relation reads

$$\mathrm{div}\,\mathbf{u} = \mathrm{tr}\,\mathbf{H} = 0. \tag{11}$$

Accordingly, the incremental forms of the boundary conditions (6) are

$$\dot{\mathbf{T}}_0^{\mathrm{T}}\mathbf{n} = \dot{\mathbf{t}}_{A0}, \quad \dot{\mathbf{E}}_{l0} \times \mathbf{n} = \mathbf{0}, \quad \dot{\mathbf{D}}_{l0} \cdot \mathbf{n} = \dot{q}_e, \tag{12}$$

where $\dot{\mathbf{t}}_{A0}$ and $\dot{q}_e$ are the incremental mechanical traction and surface charge density per unit area of ∂B_t, respectively.

(a). Reference configuration

(b). Current configuration
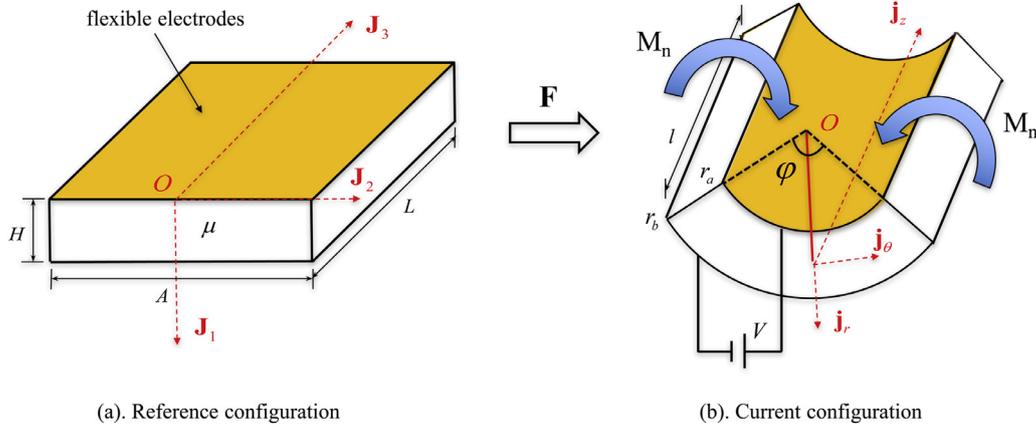
Fig. 2. Sketch of a dielectric slab with a voltage applied across its thickness subject to finite bending.

3. Finite bending and associated stability analysis

3.1. Finite bending deformation

We consider an initially undeformed dielectric slab of length L, thickness H and width A, with two flexible electrodes (carbon grease for example) glued onto its top and bottom faces. We assume the electrodes to be so thin and soft that their mechanical role can be ignored during the deformation.

The width and length aspect ratios of the slab are A/H and L/H, respectively. The slab originally occupies the region

$$0 \leq X_1 \leq H, \quad -\frac{A}{2} \leq X_2 \leq \frac{A}{2}, \quad 0 \leq X_3 \leq L, \quad (13)$$

as depicted in Fig. 2(a). With the application of a voltage through the thickness and of mechanical loads (later calculations show that only moments are needed for the bending), the slab bends into the current region

$$r_a \leq r \leq r_b, \quad -\frac{\varphi}{2} \leq \theta \leq \frac{\varphi}{2}, \quad 0 \leq z \leq l, \quad (14)$$

as depicted in Fig. 2(b), through the following bending deformation (Green and Zerna, 1954; Ogden, 1997)

$$r = \sqrt{d + \frac{2X_1}{\omega}}, \quad \theta = \frac{\omega X_2}{\lambda_z}, \quad z = \lambda_z X_3, \quad (15)$$

where (X_1, X_2, X_3) and (r, θ, z) are the rectangular Cartesian and cylindrical coordinates in the reference and deformed configurations, with orthogonal bases $(\mathbf{J}_1, \mathbf{J}_2, \mathbf{J}_3)$ and $(\mathbf{j}_r, \mathbf{j}_\theta, \mathbf{j}_z)$, respectively. In Eq. (15), d and ω are constants to be determined, λ_z is the axial principal stretch, which is taken to be prescribed, l, r_a, r_b and φ are the length, inner and outer radii and the bending angle of the deformed sector, respectively, given by

$$l = \lambda_z L, \quad r_a = \sqrt{d}, \quad r_b = \sqrt{d + \frac{2H}{\omega}}, \quad \varphi = \frac{\omega A}{\lambda_z}. \quad (16)$$

Then the deformation gradient has the following components in the $\mathbf{J}_i \otimes \mathbf{j}_\alpha (i = 1, 2, 3 \text{ and } \alpha = r, \theta, z)$ basis,

$$\mathbf{F} = \begin{bmatrix} \lambda^{-1}\lambda_z^{-1} & 0 & 0 \\ 0 & \lambda & 0 \\ 0 & 0 & \lambda_z \end{bmatrix}, \quad (17)$$

with $\lambda = \omega r/\lambda_z$ being the circumferential principal stretch. Combining Eqs. (16) and (17), we establish the following relationships,

$$\omega = \frac{\lambda_z^2(\lambda_b^2 - \lambda_a^2)}{2H}, \quad \varphi = \frac{\lambda_z(\lambda_b^2 - \lambda_a^2)}{2}\frac{A}{H}, \quad (18)$$

where $\lambda_a = \omega r_a/\lambda_z, \lambda_b = \omega r_b/\lambda_z$ are the circumferential stretches of the inner and outer surfaces of the deformed sector, respectively.

Now assume that the nominal electric field and electric displacement in the reference configuration are transverse,

$$\mathbf{E}_l = \begin{bmatrix} E_0 & 0 & 0 \end{bmatrix}^\mathrm{T}, \quad \mathbf{D}_l = \begin{bmatrix} D_0 & 0 & 0 \end{bmatrix}^\mathrm{T}, \quad (19)$$

where E_0 and D_0 are the only non-zero components of the nominal electric field and electric displacement, respectively. Then the true electric field and electric displacement in the deformed configuration are

$$\mathbf{E} = \mathbf{F}^{-T}\mathbf{E}_l = \begin{bmatrix} E_r & 0 & 0 \end{bmatrix}^\mathrm{T}, \quad \mathbf{D} = \mathbf{F}\mathbf{D}_l = \begin{bmatrix} D_r & 0 & 0 \end{bmatrix}^\mathrm{T}, \quad (20)$$

where $E_r = \lambda\lambda_z E_0 = E_0\omega r$ and $D_r = \lambda^{-1}\lambda_z^{-1}D_0 = D_0/(\omega r)$. The Maxwell equation $(5)_3$ reads

$$\frac{\partial D_r}{\partial r} + \frac{1}{r}D_r = \frac{1}{r}\frac{\partial (rD_r)}{\partial r} = 0, \quad (21)$$

showing that D_0 is a constant. Notice, however, that E_0 is not a constant.

According to Eq. (2), the invariants are

$$I_1 = \lambda^2 + \lambda^{-2}\lambda_z^{-2} + \lambda_z^2, \quad I_2 = \lambda^{-2} + \lambda^2\lambda_z^2 + \lambda_z^{-2},$$
$$I_4 = D_0^2, \quad I_5 = \lambda^{-2}\lambda_z^{-2}D_0^2, \quad I_6 = \lambda^{-4}\lambda_z^{-4}D_0^2. \quad (22)$$

From Eqs. (3) and (4), we further obtain the non-zero components of the Cauchy stress $\boldsymbol{\tau}$ and of the electric field $\mathbf{E}$ as

$$\tau_{rr} = 2\lambda^{-2}\lambda_z^{-2}\Omega_1 + 2(\lambda^{-2} + \lambda_z^{-2})\Omega_2 + 2\lambda^{-2}\lambda_z^{-2}D_0^2\Omega_5$$
$$+ 4\lambda^{-4}\lambda_z^{-4}D_0^2\Omega_6 - p,$$
$$\tau_{\theta\theta} = 2\lambda^2\Omega_1 + 2(\lambda_z^{-2} + \lambda^2\lambda_z^2)\Omega_2 - p,$$
$$\tau_{zz} = 2\lambda_z^2\Omega_1 + 2(\lambda^{-2} + \lambda^2\lambda_z^2)\Omega_2 - p, \quad (23)$$

$$E_r = 2(\lambda^2\lambda_z^2\Omega_4 + \Omega_5 + \lambda^{-2}\lambda_z^{-2}\Omega_6)D_r$$
$$= 2(\lambda\lambda_z\Omega_4 + \lambda^{-1}\lambda_z^{-1}\Omega_5 + \lambda^{-3}\lambda_z^{-3}\Omega_6)D_0. \quad (24)$$

At this stage we note that the energy function has only three independent variables: λ, λ_z and D_0. Introducing a reduced energy function W defined by

$$W(\lambda, \lambda_z, D_0) = \Omega(I_1, I_2, I_4, I_5, I_6). \quad (25)$$

Eqs. (23) and (24) can be rewritten compactly as

$$\tau_{rr} - \tau_{\theta\theta} = -\lambda\frac{\partial W}{\partial \lambda}, \quad (26)$$

$$E_0 = \lambda^{-1}\lambda_z^{-1}E_r = \frac{\partial W}{\partial D_0}. \quad (27)$$

For the considered deformation, the equilibrium Eq. (5)$_1$ reduces to the radial component equation

$$\frac{\partial \tau_{rr}}{\partial r} + \frac{1}{r}(\tau_{rr} - \tau_{\theta\theta}) = 0. \tag{28}$$

Combining Eqs. (26) and (28) and using the relation $d\lambda/\lambda = dr/r$ enables us to rewrite the principal stress components τ_{rr} and $\tau_{\theta\theta}$ as

$$\tau_{rr} = W + K, \tag{29}$$

$$\tau_{\theta\theta} = \lambda \frac{\partial W}{\partial \lambda} + \tau_{rr} = \lambda \frac{\partial W}{\partial \lambda} + W + K, \tag{30}$$

where K is a constant to be determined from the boundary conditions. Here the inner and outer surfaces at r_a and r_b are free of mechanical tractions, so that

$$\tau_{rr}(r_a) = \tau_{rr}(r_b) = 0. \tag{31}$$

Then the constant K can be obtained as

$$K = -W(\lambda_a, \lambda_z, D_0) = -W(\lambda_b, \lambda_z, D_0), \tag{32}$$

and the connection between λ_a, λ_b, λ_z and D_0 can be established as

$$W(\lambda_a, \lambda_z, D_0) - W(\lambda_b, \lambda_z, D_0) = 0. \tag{33}$$

According to Eq. (5)$_2$, the electric field can be expressed as $\boldsymbol{E} = -\mathrm{grad}\phi$, where ϕ is the electric potential, with the only non-zero radial electric field component given by $E_r = -d\phi/dr$. We denote the electric voltage difference between the inner and outer surfaces as $V = \phi_a - \phi_b$, which, with the help of Eqs. (18)$_1$ and (27), can be obtained as

$$V = \int_{r_a}^{r_b} \lambda \lambda_z \frac{\partial W}{\partial D_0}\, dr = \frac{\lambda_z^2}{\omega} \int_{\lambda_a}^{\lambda_b} \lambda \frac{\partial W}{\partial D_0}\, d\lambda = \frac{2H}{\lambda_b^2 - \lambda_a^2} \int_{\lambda_a}^{\lambda_b} \lambda \frac{\partial W}{\partial D_0}\, d\lambda. \tag{34}$$

Eq. (34) provides the equilibrium relation between the constants V, D_0, λ_a, λ_b and λ_z, once the energy function of the material is specified.

Then by solving the Eqs. (18)$_2$, (33) and (34), λ_a, λ_b and D_0 can be determined once V, φ, λ_z and A/H are given. Eventually the inner and outer radii of the deformed sector r_a and r_b, the constant ω and the circumferential principal stretch of arbitrary point in the sector λ can be derived as

$$r_a = \frac{\lambda_a \lambda_z}{\omega} = \frac{\lambda_a}{\varphi}A, \quad r_b = \frac{\lambda_b \lambda_z}{\omega} = \frac{\lambda_b}{\varphi}A, \quad \omega = \frac{\lambda_z \varphi}{A}, \quad \lambda = \frac{\omega r}{\lambda_z}. \tag{35}$$

As a result, the configuration and the distributions of stretches of the deformed sector are fully determined. Finally, the required applied axial force F_N and the moment M_n about the origin on the lateral faces $\theta = \pm \omega A/(2\lambda_z)$ can be determined as

$$F_N = \lambda_z L \int_{r_a}^{r_b} \tau_{\theta\theta}\, dr = \frac{2HL}{\lambda_b^2 - \lambda_a^2} \int_{\lambda_a}^{\lambda_b} \tau_{\theta\theta}\, d\lambda = \mu HL \overline{F}_N,$$

$$M_n = \lambda_z L \int_{r_a}^{r_b} r\tau_{\theta\theta}\, dr = \frac{4H^2 L}{\lambda_z(\lambda_b^2 - \lambda_a^2)^2} \int_{\lambda_a}^{\lambda_b} \lambda \tau_{\theta\theta}\, d\lambda = \mu H^2 L \overline{M}_n, \tag{36}$$

where μ is the initial mechanical shear modulus, $\overline{F}_N$ and $\overline{M}_n$ are dimensionless measures of the axial force and moment, respectively. Note that from Eq. (28) we have the relation $\tau_{\theta\theta} = d(r\tau_{rr})/(dr)$, thus Eq. (36)$_1$ reads

$$F_N = \frac{2HL}{\lambda_b^2 - \lambda_a^2} \int_{r_a}^{r_b} \tau_{\theta\theta}\, dr = \frac{2HL}{\lambda_b^2 - \lambda_a^2}[r_b \tau_{rr}(r_b) - r_a \tau_{rr}(r_a)], \tag{37}$$

which identically equals to zero due to the boundary condition (31). Hence, only moments are required to bend the slab.

3.2. Small-amplitude wrinkle

We now superimpose a small harmonic inhomogeneous deformation on the underlying deformed configuration of the sector, to model the onset of wrinkling on the inner curved face.

We start with the components of the incremental displacement and the incremental electric displacement in the form

$$u_i = u_i(r, \theta, z), \quad \dot{D}_{l0i} = \dot{D}_{l0i}(r, \theta, z). \tag{38}$$

Then the incremental displacement gradient reads

$$\boldsymbol{H} = \begin{bmatrix} \frac{\partial u_r}{\partial r} & \frac{1}{r}\left(\frac{\partial u_r}{\partial \theta} - u_\theta\right) & \frac{\partial u_r}{\partial z} \\ \frac{\partial u_\theta}{\partial r} & \frac{1}{r}\left(\frac{\partial u_\theta}{\partial \theta} + u_r\right) & \frac{\partial u_\theta}{\partial z} \\ \frac{\partial u_z}{\partial r} & \frac{1}{r}\frac{\partial u_z}{\partial \theta} & \frac{\partial u_z}{\partial z} \end{bmatrix}, \tag{39}$$

in the $\boldsymbol{j}_\alpha \otimes \boldsymbol{j}_\beta (\alpha, \beta = r, \theta, z)$ basis, and the incompressibility condition Eq. (11) for the incremental motion reads

$$\mathrm{div}\boldsymbol{u} = \mathrm{tr}\boldsymbol{H} = \frac{\partial u_r}{\partial r} + \frac{1}{r}\left(\frac{\partial u_\theta}{\partial \theta} + u_r\right) + \frac{\partial u_z}{\partial z} = 0. \tag{40}$$

From Eq. (10)$_2$, we introduce an incremental electric potential $\dot{\phi}$, and the components of the incremental electric field are

$$\dot{E}_{l0r} = -\frac{\partial \dot{\phi}}{\partial r}, \quad \dot{E}_{l0\theta} = -\frac{1}{r}\frac{\partial \dot{\phi}}{\partial \theta}, \quad \dot{E}_{l0z} = -\frac{\partial \dot{\phi}}{\partial z}. \tag{41}$$

Now the electro-elastic moduli tensors $\boldsymbol{A}_0$, $\boldsymbol{\Gamma}_0$ and $\boldsymbol{K}_0$ can be evaluated according to Eq. (8), with non-zero components listed in Appendix A. Then the components of the incremental stress and electric fields are expanded as (Wu et al., 2017)

$$\dot{T}_{0rr} = (A_{01111} + p)\frac{\partial u_r}{\partial r} + A_{01122}\frac{1}{r}\left(\frac{\partial u_\theta}{\partial \theta} + u_r\right) + A_{01133}\frac{\partial u_z}{\partial z}$$
$$+ \Gamma_{0111}\dot{D}_{l0r} - \dot{p},$$

$$\dot{T}_{0\theta\theta} = A_{01122}\frac{\partial u_r}{\partial r} + (A_{02222} + p)\frac{1}{r}\left(\frac{\partial u_\theta}{\partial \theta} + u_r\right) + A_{02233}\frac{\partial u_z}{\partial z}$$
$$+ \Gamma_{0221}\dot{D}_{l0r} - \dot{p},$$

$$\dot{T}_{0zz} = A_{01133}\frac{\partial u_r}{\partial r} + A_{02233}\frac{1}{r}\left(\frac{\partial u_\theta}{\partial \theta} + u_r\right) + (A_{03333} + p)\frac{\partial u_z}{\partial z}$$
$$+ \Gamma_{0331}\dot{D}_{l0r} - \dot{p},$$

$$\dot{T}_{0r\theta} = A_{01212}\frac{\partial u_\theta}{\partial r} + (A_{01221} + p)\frac{1}{r}\left(\frac{\partial u_r}{\partial \theta} - u_\theta\right) + \Gamma_{0122}\dot{D}_{l0\theta},$$

$$\dot{T}_{0rz} = A_{01313}\frac{\partial u_z}{\partial r} + (A_{01331} + p)\frac{\partial u_r}{\partial z} + \Gamma_{0133}\dot{D}_{l0z},$$

$$\dot{T}_{0\theta r} = A_{02121}\frac{1}{r}\left(\frac{\partial u_r}{\partial \theta} - u_\theta\right) + (A_{01221} + p)\frac{\partial u_\theta}{\partial r} + \Gamma_{0122}\dot{D}_{l0\theta},$$

$$\dot{T}_{0\theta z} = A_{2323}\frac{1}{r}\frac{\partial u_z}{\partial \theta} + (A_{02332} + p)\frac{\partial u_\theta}{\partial z},$$

$$\dot{T}_{0zr} = A_{03131}\frac{\partial u_r}{\partial z} + (A_{01331} + p)\frac{\partial u_z}{\partial r} + \Gamma_{0133}\dot{D}_{l0z},$$

$$\dot{T}_{0z\theta} = A_{03232}\frac{\partial u_\theta}{\partial z} + (A_{02332} + p)\frac{1}{r}\frac{\partial u_z}{\partial \theta}, \tag{42}$$

and

$$\dot{E}_{l0r} = -\frac{\partial \dot{\phi}}{\partial r} = \Gamma_{0111}\frac{\partial u_r}{\partial r} + \Gamma_{221}\frac{1}{r}\left(\frac{\partial u_\theta}{\partial \theta} + u_r\right) + \Gamma_{0331}\frac{\partial u_z}{\partial z} + K_{011}\dot{D}_{l0r},$$

$$\dot{E}_{l0\theta} = -\frac{1}{r}\frac{\partial \dot{\phi}}{\partial \theta} = \Gamma_{0122}\left[\frac{1}{r}\left(\frac{\partial u_r}{\partial \theta} - u_\theta\right) + \frac{\partial u_\theta}{\partial r}\right] + K_{022}\dot{D}_{l0\theta},$$

$$\dot{E}_{l0z} = -\frac{\partial \dot{\phi}}{\partial z} = \Gamma_{0133}\left(\frac{\partial u_r}{\partial z} + \frac{\partial u_z}{\partial_r}\right) + K_{033}\dot{D}_{l0z}, \tag{43}$$

according to Eq. (7).

Finally, the incremental forms of equilibrium Eq. (10)$_1$ and the incremental Maxwell Eq. (10)$_3$ reduce to

$$\frac{\partial \dot{T}_{0rr}}{\partial r} + \frac{1}{r}\frac{\partial \dot{T}_{0\theta r}}{\partial \theta} + \frac{\dot{T}_{0rr} - \dot{T}_{0\theta\theta}}{r} + \frac{\partial \dot{T}_{0zr}}{\partial z} = 0,$$

$$\frac{\partial \dot{T}_{0r\theta}}{\partial r} + \frac{1}{r}\frac{\partial \dot{T}_{0\theta\theta}}{\partial \theta} + \frac{\dot{T}_{0\theta r} + \dot{T}_{0r\theta}}{r} + \frac{\partial \dot{T}_{0z\theta}}{\partial z} = 0,$$

$$\frac{\partial \dot{T}_{0rz}}{\partial r} + \frac{1}{r}\frac{\partial \dot{T}_{0\theta z}}{\partial \theta} + \frac{\partial \dot{T}_{0zz}}{\partial z} + \frac{\dot{T}_{0rz}}{r} = 0, \tag{44}$$

and

$$\frac{\partial \dot{D}_{l0r}}{\partial r} + \frac{1}{r}\left(\frac{\partial \dot{D}_{l0\theta}}{\partial \theta} + \dot{D}_{l0r}\right) + \frac{\partial \dot{D}_{l0z}}{\partial z} = 0, \tag{45}$$

respectively.

We assume that the sector is under end thrust at the lateral faces $\theta = \pm\omega A/(2\lambda_z)$ and $z = 0, l$, while the two surfaces $r = r_a, r_b$ remain traction-free and the applied voltage is taken to be a constant. The boundary conditions for the incremental fields are

$$u_\theta = \dot{T}_{0\theta r} = \dot{T}_{0\theta z} = 0 \qquad\qquad\qquad \text{at} \quad \theta = \pm\omega A/(2\lambda_z),$$

$$u_z = \dot{T}_{0zr} = \dot{T}_{0z\theta} = 0 \qquad\qquad\qquad \text{at} \quad z = 0, \lambda_z L,$$

$$\dot{T}_{0rr} = \dot{T}_{0r\theta} = \dot{T}_{0rz} = \dot{\phi} = 0 \qquad\qquad \text{at} \quad r = r_a, r_b. \tag{46}$$

3.3. Stroh formulation

We seek solutions of equations in Section 3.2 in the form (Su et al., 2016b)

$$u_r = U_r(r)\cos(n\theta)\cos(kz), \qquad\qquad\qquad u_\theta = U_\theta(r)\sin(n\theta)\cos(kz),$$

$$u_z = U_z(r)\cos(n\theta)\sin(kz), \qquad\qquad\qquad \dot{\phi} = \Phi(r)\cos(n\theta)\cos(kz),$$

$$\dot{T}_{0rr} = \Sigma_{rr}(r)\cos(n\theta)\cos(kz), \qquad\qquad\quad \dot{T}_{0r\theta} = \Sigma_{r\theta}(r)\sin(n\theta)\cos(kz),$$

$$\dot{T}_{0rz} = \Sigma_{rz}(r)\cos(n\theta)\sin(kz), \qquad\qquad\quad \dot{D}_{l0r} = \Delta_r(r)\cos(n\theta)\cos(kz), \tag{47}$$

where n and k are the circumferential and axial wave numbers, respectively. Then from the incremental constitutive equations (42), (43) and the incremental boundary conditions (46)$_{1,2}$, we have

$$n = \frac{2\lambda_z q\pi}{\omega A} = \frac{4q\pi}{\lambda_z(\lambda_b^2 - \lambda_a^2)}\frac{H}{A}, \quad k = \frac{m\pi}{\lambda_z L} \quad (q, m = 0, 1, 2, \ldots), \tag{48}$$

where the positive integers q and m give the numbers of circumferential and axial wrinkles of the sector, respectively (Destrade et al., 2009b; Balbi et al., 2015). It should be noticed that they cannot be zero simultaneously.

Then Eqs. (40)–(45) that govern the incremental motion of the dielectric sector can be rearranged to yield the following first-order differential system (Destrade et al., 2009a,b, 2014; Balbi et al., 2015)

$$\frac{d}{dr}\boldsymbol{\eta}(r) = \frac{1}{r}\boldsymbol{G}(r)\boldsymbol{\eta}(r), \tag{49}$$

where

$$\boldsymbol{\eta}(r) = \begin{bmatrix} U_r & U_\theta & U_z & r\Delta_r & r\Sigma_{rr} & r\Sigma_{r\theta} & r\Sigma_{rz} & \Phi \end{bmatrix}^\mathrm{T} = \begin{bmatrix} \boldsymbol{U} & \boldsymbol{S} \end{bmatrix}^\mathrm{T}, \tag{50}$$

is the Stroh vector (with $\boldsymbol{U} = \begin{bmatrix} U_r & U_\theta & U_z & r\Delta_r \end{bmatrix}^\mathrm{T}$ and $\boldsymbol{S} = \begin{bmatrix} r\Sigma_{rr} & r\Sigma_{r\theta} & r\Sigma_{rz} & \Phi \end{bmatrix}^\mathrm{T}$), $\boldsymbol{G}$ is the so-called Stroh matrix, which has the following block structure

$$\boldsymbol{G} = \begin{bmatrix} \boldsymbol{G}_1 & \boldsymbol{G}_2 \\ \boldsymbol{G}_3 & \boldsymbol{G}_4 \end{bmatrix}, \tag{51}$$

where the four 4×4 sub-blocks $\boldsymbol{G}_1$, $\boldsymbol{G}_2$, $\boldsymbol{G}_3$ and $\boldsymbol{G}_4$ have the following components

$$
G_1 = \begin{bmatrix} -1 & -n & -kr & 0 \\ \frac{n(\gamma_{12}-\tau_{rr})}{\gamma_{12}} & \frac{\gamma_{12}-\tau_{rr}}{\gamma_{12}} & 0 & 0 \\ \frac{kr(\gamma_{13}-\tau_{rr})}{\gamma_{13}} & 0 & 0 & 0 \\ \xi_1 & -\frac{n\tau_{rr}}{\gamma_{12}}\frac{\Gamma_{0122}}{K_{022}} & 0 & 0 \end{bmatrix}, \quad
G_2 = \begin{bmatrix} 0 & 0 & 0 & 0 \\ 0 & \frac{1}{\gamma_{12}} & 0 & -\frac{n}{\gamma_{12}}\frac{\Gamma_{0122}}{K_{022}} \\ 0 & 0 & \frac{1}{\gamma_{13}} & -\frac{kr}{\gamma_{13}}\frac{\Gamma_{0133}}{K_{033}} \\ 0 & \frac{n}{\gamma_{12}}\frac{\Gamma_{0122}}{K_{022}} & \frac{kr}{\gamma_{13}}\frac{\Gamma_{0133}}{K_{033}} & \xi_2 \end{bmatrix},
$$

$$
G_3 = \begin{bmatrix} \kappa_{11} & \kappa_{12} & \kappa_{13} & -(\Gamma_{0111}-\Gamma_{0221}) \\ \kappa_{12} & \kappa_{22} & \kappa_{23} & -n(\Gamma_{0111}-\Gamma_{0221}) \\ \kappa_{13} & \kappa_{23} & \kappa_{33} & -kr(\Gamma_{0111}-\Gamma_{0331}) \\ \Gamma_{0111}-\Gamma_{0221} & n(\Gamma_{0111}-\Gamma_{0221}) & kr(\Gamma_{0111}-\Gamma_{0331}) & -K_{011} \end{bmatrix},
$$

$$
G_4 = \begin{bmatrix} 1 & -\frac{n(\gamma_{12}-\tau_{rr})}{\gamma_{12}} & -\frac{kr(\gamma_{13}-\tau_{rr})}{\gamma_{13}} & \xi_1 \\ n & -\frac{\gamma_{12}-\tau_{rr}}{\gamma_{12}} & 0 & -\frac{n\tau_{rr}}{\gamma_{12}}\frac{\Gamma_{0122}}{K_{022}} \\ kr & 0 & 0 & 0 \\ 0 & 0 & 0 & 0 \end{bmatrix}. \tag{52}
$$

Here

$$
\gamma_{12} = A_{01212} - \frac{\Gamma_{0122}^2}{K_{022}}, \quad \gamma_{21} = A_{02121} - \frac{\Gamma_{0122}^2}{K_{022}}, \quad \gamma_{23} = A_{02323},
$$

$$
\gamma_{13} = A_{01313} - \frac{\Gamma_{0133}^2}{K_{033}}, \quad \gamma_{31} = A_{03131} - \frac{\Gamma_{0133}^2}{K_{033}}, \quad \gamma_{32} = A_{03232},
$$

$$
\xi_1 = -\left(\frac{\Gamma_{0122}}{K_{022}}\frac{n^2}{\gamma_{12}} + \frac{\Gamma_{0133}}{K_{033}}\frac{k^2 r^2}{\gamma_{13}} \right)\tau_{rr},
$$

$$
\xi_2 = -\left(\frac{n^2}{K_{022}} + \frac{\Gamma_{0122}^2}{K_{022}^2}\frac{n^2}{\gamma_{12}} + \frac{k^2 r^2}{K_{033}} + \frac{\Gamma_{0133}^2}{K_{033}^2}\frac{k^2 r^2}{\gamma_{13}} \right),
$$

$$
\beta_{12} = \frac{1}{2}\left(A_{01111} + A_{02222} - 2A_{01122} - 2A_{01221} + \frac{2\Gamma_{0122}^2}{K_{022}} \right),
$$

$$
\beta_{13} = \frac{1}{2}\left(A_{01111} + A_{03333} - 2A_{01133} - 2A_{01331} + \frac{2\Gamma_{0133}^2}{K_{033}} \right),
$$

$$
\kappa_{11} = 2(\gamma_{12} - \tau_{rr} + \beta_{12}) + n^2\left[\gamma_{21} - \frac{(\gamma_{12}-\tau_{rr})^2}{\gamma_{12}} \right] + k^2 r^2\left[\gamma_{31} - \frac{(\gamma_{13}-\tau_{rr})^2}{\gamma_{13}} \right],
$$

$$
\kappa_{12} = n\left(\gamma_{12} + \gamma_{21} + 2\beta_{12} - \frac{\tau_{rr}^2}{\gamma_{12}} \right), \quad \kappa_{13} = kr(A_{01111} + A_{02233} - A_{01122} - A_{01133} + p),
$$

$$
\kappa_{22} = 2n^2(\gamma_{12} - \tau_{rr} + \beta_{12}) + \gamma_{21} - \frac{(\gamma_{12}-\tau_{rr})^2}{\gamma_{12}} + k^2 r^2\gamma_{32},
$$

$$
\kappa_{23} = nkr(A_{01111} + A_{02233} + A_{02332} - A_{01122} - A_{01133} + 2p),
$$

$$
\kappa_{33} = 2k^2 r^2(\gamma_{13} - \tau_{rr} + \beta_{13}) + n^2\gamma_{23}. \tag{53}
$$

It should be noticed that to derive Eqs. (49)–(53), we made use of the connections

$$
A_{01221} + p = A_{01212} - \tau_{rr}, \quad A_{01331} + p = A_{01313} - \tau_{rr}, \tag{54}
$$

which result from Eqs. (8)$_1$ and (9). The derivation of the Stroh formulation is given in Appendix B.

Now the incremental boundary conditions (46)$_3$ read

$$
S(r_a) = S(r_b) = 0. \tag{55}
$$

Note that we chose to write the components of η in the order presented in Eq. (50), because it will turn out to be the most practical for those boundary value problems where the electric field is due to a constant voltage applied to the bent faces of the sector. For the case where the sector is charge-controlled (Keplinger et al., 2010; Dorfmann and Ogden, 2014a; Su et al., 2016a; 2016b) instead of voltage-controlled, the places of $r\Delta$ and Φ must be swapped in η for greater efficiency in the scheme. In other words, η and G in Eq. (49) should be replaced with $\hat{\eta}$ and $\hat{G}$, respectively, where

$$
\hat{\eta} = \begin{bmatrix} U_r \\ U_\theta \\ U_z \\ \Phi \\ r\Sigma_{rr} \\ r\Sigma_{\theta\theta} \\ r\Sigma_{zz} \\ r\Delta \end{bmatrix} = \begin{bmatrix} \hat{U} \\ \hat{S} \end{bmatrix} = R\eta, \quad \hat{G} = RGR^{-1}, \quad R = \begin{bmatrix} 1 & 0 & 0 & 0 & 0 & 0 & 0 & 0 \\ 0 & 1 & 0 & 0 & 0 & 0 & 0 & 0 \\ 0 & 0 & 1 & 0 & 0 & 0 & 0 & 0 \\ 0 & 0 & 0 & 0 & 0 & 0 & 0 & 1 \\ 0 & 0 & 0 & 0 & 1 & 0 & 0 & 0 \\ 0 & 0 & 0 & 0 & 0 & 1 & 0 & 0 \\ 0 & 0 & 0 & 0 & 0 & 0 & 1 & 0 \\ 0 & 0 & 0 & 1 & 0 & 0 & 0 & 0 \end{bmatrix}, \tag{56}
$$

with $\hat{U} = \begin{bmatrix} U_r & U_\theta & U_z & \Phi \end{bmatrix}^T$ and $\hat{S} = \begin{bmatrix} r\Sigma_{rr} & r\Sigma_{r\theta} & r\Sigma_{rz} & r\Delta_r \end{bmatrix}^T$. Then the traction-free boundary conditions at the two surfaces r_a, r_b, Eq. (55) should be modified as

$$
\hat{S}(r_a) = \hat{S}(r_b) = 0. \tag{57}
$$

As a result, the method presented in this paper can be easily extended to the case of a charge-controlled sector. Our calculations (not presented here) show that we then recover the same results as in the literature when the slab is reduced to a half-space (Dorfmann and Ogden, 2010b).

3.4. The surface impedance matrix method

The inhomogeneous differential system (49) is stiff numerically, especially for thick slabs. Over the years, several algorithms such as the compound matrix method (Shmuel and deBotton, 2013) and the state space method (Wu et al., 2017) have been adopted to overcome the stiffness of this equation. Here the so-called surface impedance matrix method (Destrade et al., 2009a,b, 2014; Balbi et al., 2015) is employed to build a robust and efficient numerical procedure for obtaining the dispersion equation.

We introduce the 8×8 matricant $\boldsymbol{M}(r, r_a) = \begin{bmatrix} \boldsymbol{M}_1(r, r_a) & \boldsymbol{M}_2(r, r_a) \\ \boldsymbol{M}_3(r, r_a) & \boldsymbol{M}_4(r, r_a) \end{bmatrix}$, which is defined as the matrix such that

$$\boldsymbol{\eta}(r) = \boldsymbol{M}(r, r_a)\boldsymbol{\eta}(r_a), \tag{58}$$

with the obvious condition that

$$\boldsymbol{M}(r_a, r_a) = \boldsymbol{I}_{8\times 8}. \tag{59}$$

Use of the incremental boundary condition $\boldsymbol{S}(r_a) = 0$ gives

$$\boldsymbol{S}(r) = \boldsymbol{z}^a(r, r_a)\boldsymbol{U}(r), \tag{60}$$

where $\boldsymbol{z}^a(r, r_a)$ is the conditional impedance matrix, which is defined as

$$\boldsymbol{z}^a(r, r_a) = \boldsymbol{M}_3(r, r_a)\boldsymbol{M}_1^{-1}(r, r_a). \tag{61}$$

Substituting Eq. (60) into Eq. (49) gives

$$\frac{\mathrm{d}}{\mathrm{d}r}\boldsymbol{U} = \frac{1}{r}\boldsymbol{G}_1\boldsymbol{U} + \frac{1}{r}\boldsymbol{G}_2\boldsymbol{z}^a\boldsymbol{U}, \quad \frac{\mathrm{d}}{\mathrm{d}r}(\boldsymbol{z}^a\boldsymbol{U}) = \frac{1}{r}\boldsymbol{G}_3\boldsymbol{U} + \frac{1}{r}\boldsymbol{G}_4\boldsymbol{z}^a\boldsymbol{U}. \tag{62}$$

Elimination of $\boldsymbol{U}$ from Eq. (62) yields the following Riccati differential equation

$$\frac{\mathrm{d}\boldsymbol{z}^a}{\mathrm{d}r} = \frac{1}{r}(-\boldsymbol{z}^a\boldsymbol{G}_1 - \boldsymbol{z}^a\boldsymbol{G}_2\boldsymbol{z}^a + \boldsymbol{G}_3 + \boldsymbol{G}_4\boldsymbol{z}^a), \tag{63}$$

with the initial condition

$$\boldsymbol{z}^a(r_a, r_a) = \boldsymbol{0}, \tag{64}$$

which follows from Eqs. (59) and (61).

Then we integrate Eq. (63) numerically with the initial condition (64) from r_a to r_b and tune the bending angle until the following target condition is satisfied

$$\det \boldsymbol{z}^a(r_b, r_a) = 0, \tag{65}$$

which results from the boundary

$$\boldsymbol{S}(r_b) = \boldsymbol{z}^a(r_b, r_a)\boldsymbol{U}(r_b) = \boldsymbol{0}. \tag{66}$$

The conclusion is that, for a given voltage V, the critical bending angle φ_c can be determined, and so can the critical value of the inner circumferential stretch λ_a, which we denote by λ_c.

It follows from Eq. (66) that the ratios of the incremental motion on the outer face of the sector can be determined as

$$t_\theta = \frac{U_\theta(r_b)}{U_r(r_b)}$$
$$= \frac{Q_{11}Q_{24}Q_{33} + Q_{13}Q_{21}Q_{34} + Q_{14}Q_{23}Q_{31} - Q_{11}Q_{23}Q_{34} - Q_{13}Q_{24}Q_{31} - Q_{14}Q_{21}Q_{33}}{Q_{12}Q_{23}Q_{34} + Q_{13}Q_{24}Q_{32} + Q_{14}Q_{22}Q_{33} - Q_{12}Q_{24}Q_{33} - Q_{13}Q_{22}Q_{34} - Q_{14}Q_{23}Q_{32}},$$
$$t_z = \frac{U_z(r_b)}{U_r(r_b)}$$
$$= \frac{Q_{11}Q_{22}Q_{34} + Q_{12}Q_{24}Q_{31} + Q_{14}Q_{21}Q_{32} - Q_{11}Q_{24}Q_{32} - Q_{12}Q_{21}Q_{34} - Q_{14}Q_{22}Q_{31}}{Q_{12}Q_{23}Q_{34} + Q_{13}Q_{24}Q_{32} + Q_{14}Q_{22}Q_{33} - Q_{12}Q_{24}Q_{33} - Q_{13}Q_{22}Q_{34} - Q_{14}Q_{23}Q_{32}},$$
$$t_\Phi = \frac{\Phi(r_b)}{U_r(r_b)}$$
$$= \frac{Q_{11}Q_{23}Q_{32} + Q_{12}Q_{21}Q_{33} + Q_{13}Q_{22}Q_{31} - Q_{11}Q_{22}Q_{33} - Q_{12}Q_{23}Q_{31} - Q_{13}Q_{21}Q_{32}}{Q_{12}Q_{23}Q_{34} + Q_{13}Q_{24}Q_{32} + Q_{14}Q_{22}Q_{33} - Q_{12}Q_{23}Q_{31} - Q_{12}Q_{23}Q_{31} - Q_{13}Q_{21}Q_{32}}, \tag{67}$$

where the shorthand notation $Q_{ij} = z^a_{ij}(r_b, r_a)(i, j = 1, 2, 3, 4)$ is used.

On the other hand, we can also start at the outer surface $r = r_b$ and introduce the 8×8 matricant $\boldsymbol{M}(r, r_b) = \begin{bmatrix} \boldsymbol{M}_1(r, r_b) & \boldsymbol{M}_2(r, r_b) \\ \boldsymbol{M}_3(r, r_b) & \boldsymbol{M}_4(r, r_b) \end{bmatrix}$

such that

$$\boldsymbol{\eta}(r) = \boldsymbol{M}(r, r_b)\boldsymbol{\eta}(r_b), \tag{68}$$

with the obvious condition that

$$M(r_b, r_b) = I_{8 \times 8}. \tag{69}$$

Following the same procedure, we can also obtain a Riccati differential equation for the other conditional impedance matrix $z^b(r, r_b)$, as

$$\frac{dz^b}{dr} = \frac{1}{r}\left(-z^b G_1 - z^b G_2 z^b + G_3 + G_4 z^b\right). \tag{70}$$

The corresponding form of Eq. (62)$_1$ is

$$\frac{d}{dr}U = \frac{1}{r}G_1 U + \frac{1}{r}G_2 z^b U. \tag{71}$$

With the critical stretch λ_c obtained by integrating the Riccati differential equation for the $z^a(r, r_a)$ conditional impedance matrix, we can now integrate simultaneously Eqs. (70) and (71) from r_b to r_a with the following initial conditions

$$U(r_b) = U(r_b)\begin{bmatrix} 1 & t_\theta & t_z & t_\Phi \end{bmatrix}^T, \quad z^b(r_b, r_b) = 0, \tag{72}$$

to determine the full distribution of the incremental field U in the deformed sector and corresponding buckling pattern.

4. Numerical results and discussion

For illustration, we now consider the so-called ideal neo-Hookean dielectric model:

$$W = \frac{\mu}{2}\left(\lambda^2 + \lambda^{-2}\lambda_z^{-2} + \lambda_z^{-2} - 3\right) + \frac{1}{2\varepsilon}\lambda^{-2}\lambda_z^{-2}D_0^2, \tag{73}$$

where ε is the permittivity of the solid, which is independent of the deformation.

4.1. Static deformation

In this case Eqs. (18)$_2$, (33) and (34) reduce to

$$\varphi = \frac{\lambda_z(\lambda_b^2 - \lambda_a^2)}{2}\frac{A}{H}, \quad \lambda_a^2\lambda_b^2\lambda_z^2 = \overline{D}_0^2 + 1, \quad \overline{V} = \frac{2\overline{D}_0}{\lambda_z^2(\lambda_b^2 - \lambda_a^2)}\ln\frac{\lambda_b}{\lambda_a}, \tag{74}$$

where we are using the following non-dimensional measures of voltage and electric vector,

$$\overline{V} = \frac{V}{H}\sqrt{\frac{\varepsilon}{\mu}}, \quad \overline{D}_0 = \frac{D_0}{\sqrt{\mu\varepsilon}}. \tag{75}$$

For given $\overline{V}, \varphi, \lambda_z$ and A/H, λ_a, λ_b and $\overline{D}_0$ can be determined from Eq. (74). Then the dimensionless stresses and electric field in the solid follow from Eqs. (27), (29), (30) and (32) as

$$\overline{\tau}_{rr}(\lambda) = \frac{\tau_{rr}}{\mu} = \frac{(\lambda^2 - \lambda_a^2)(\lambda^2 - \lambda_b^2)}{2\lambda^2}, \quad \overline{\tau}_{\theta\theta}(\lambda) = \frac{\tau_{\theta\theta}}{\mu} = \frac{3\lambda^4 - \lambda_a^2\lambda_b^2 - \lambda^2(\lambda_a^2 + \lambda_b^2)}{2\lambda^2}, \tag{76}$$

$$\overline{E}_r = E_r\sqrt{\frac{\varepsilon}{\mu}} = \lambda^{-1}\lambda_z^{-1}\overline{D}_0. \tag{77}$$

4.1.1. Effect of the voltage

In Fig. 3 we plot the circumferential stretches of the bent inner and outer surfaces λ_a and λ_b versus the bending angle φ for different applied voltages $\overline{V} = 0, 0.5, 0.7$, based on Eq. (74). In Fig. 4, we plot the distributions of circumferential stretch λ and stress $\overline{\tau}_{\theta\theta}$ in the sector and the bending shapes for several given φ and $\overline{V}$. We can see from Eq. (74) that the length aspect ratio L/H does not affect the bending deformation of the slab. Here in the calculation the axial constraint and the initial configuration of the slab are fixed as $\lambda_z = 1, A/H = 3$, and the non-dimensional measure of the radial coordinate $\overline{r} = (r - r_a)/(r_b - r_a)$ is introduced.

It can be seen from Fig. 3 that when there is no applied voltage ($\overline{V} = 0$), the slab bends with λ_a decreasing and λ_b increasing from 1. Hence, the inner face of the sector contracts circumferentially while the outer face stretches (Fig. 4a), a result which is independent of the value of φ. With the application of voltage, both λ_a and λ_b of a slightly bent sector are larger than 1 and hence, every circumferential element in the sector is stretched (Fig. 4b). If the bending moments are increased, the bending angle increases, and the inner surface eventually contracts circumferentially, and the outer surface is stretched at all times (Fig. 4c). Note that for a bent sector, $\overline{\tau}_{\theta\theta}$ depends on $\overline{r}$ almost linearly, the transverse stress of the inner part of the sector is always compressive while that of the outer part is always tensile, separated by a neutral axis corresponding to $\overline{\tau}_{\theta\theta} = 0$.

We learn from Eq. (37) that only mechanical moments are required to drive the bending of the dielectric slab. The effect of the applied voltage $\overline{V}$ on the moment $\overline{M}_n$ needed to trigger a specific bending ($\varphi = 1, 2, 3$) of the dielectric slab with $\lambda_z = 1, A/H = 3$ is presented in Fig. 5a. We can see clearly that $\overline{M}_n$ decreases as $\overline{V}$ increases, which suggests that the application of the voltage makes the slab easier to be bent. Theoretically, as the applied voltage increases, the dielectric slab thins down, making the slab easier to be bent. As a result, the moment needed for the bending decreases. For a dielectric slab undergoing plane strain deformation, the maximal electric field $\overline{V}$ applied cannot exceed the value 1 (Fig. 5b). As the electric field tends to 1, the slab becomes be ultra-thin, and the moment drops to zero (Fig. 5a).
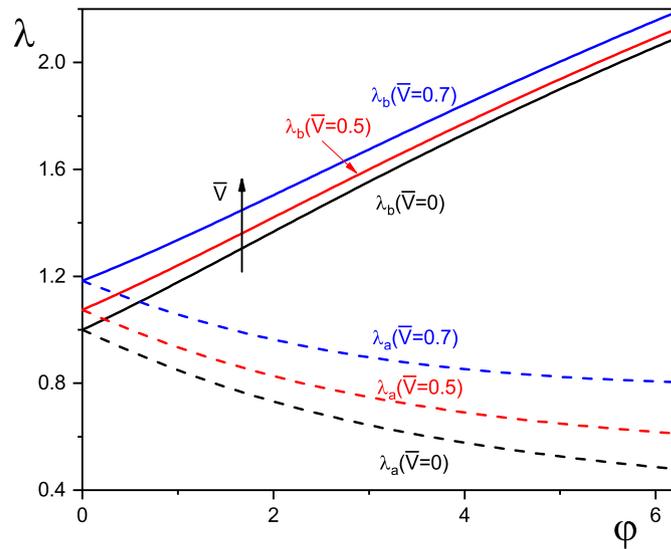
Fig. 3. Plots of $\lambda_a, \lambda_b - \varphi$ for dielectric slabs with $\lambda_z = 1, A/H = 3$ subject to voltage $\overline{V} = 0, 0.5, 0.7$, respectively.
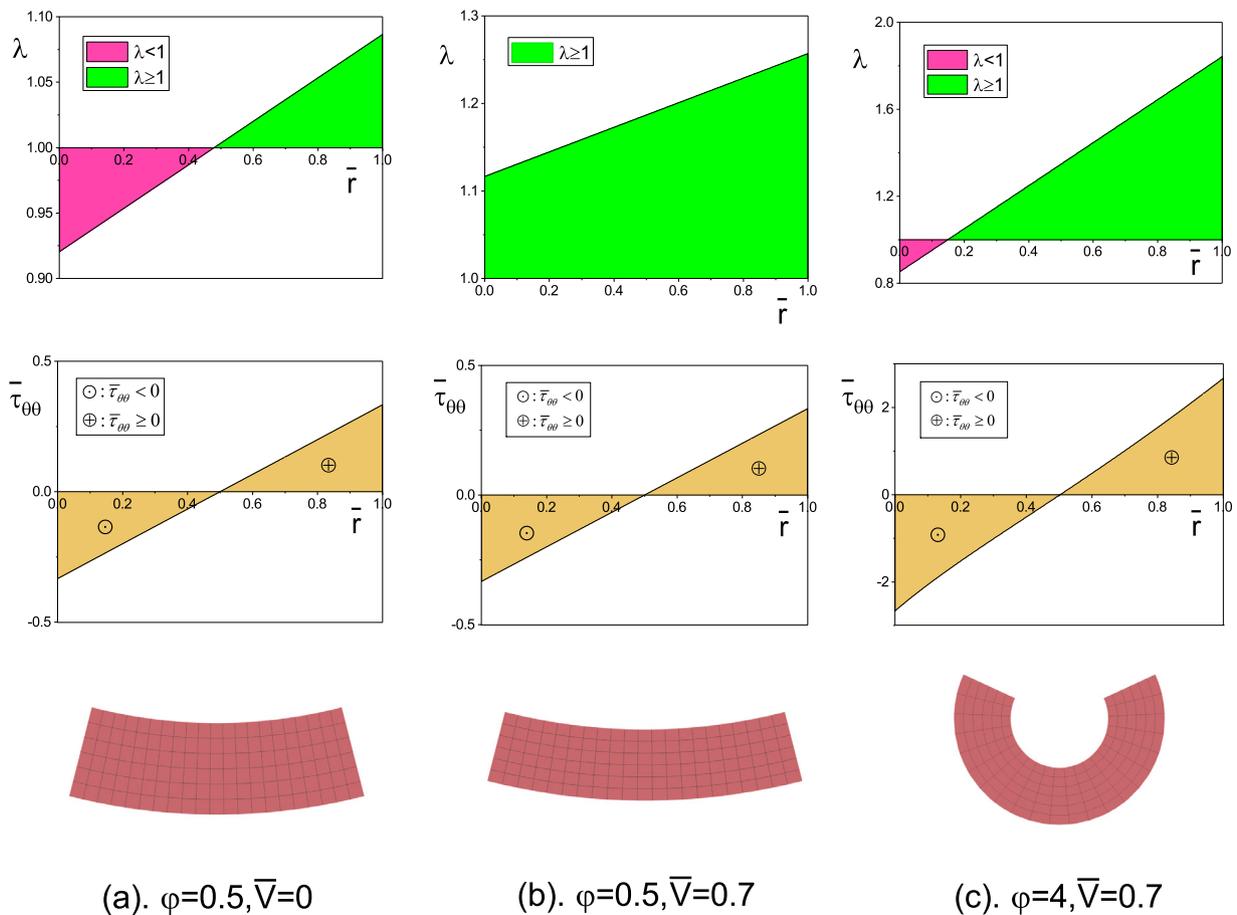
(a). $\varphi = 0.5, \overline{V} = 0$ (b). $\varphi = 0.5, \overline{V} = 0.7$ (c). $\varphi = 4, \overline{V} = 0.7$

Fig. 4. Bending of dielectric slabs which are three times wider than thick, with no axial compression ($\lambda_z = 1, A/H = 3$) and subject to various bending angles and voltage loadings: (a) $\varphi = 0.5, \overline{V} = 0$; (b) $\varphi = 0.5, \overline{V} = 0.7$; (c) $\varphi = 4, \overline{V} = 0.7$. The top, middle and bottom rows correspond to the circumferential stretch, circumferential stress distributions, and bending shapes, respectively.

4.1.2. Effect of the axial compression

Figs. 6–9 illustrate the effect of the axial constraint as measured by the stretch λ_z on the finite bending of a dielectric slab with $\overline{V} = 0, A/H = 3$. We see that compressive ($\lambda_z < 1$) and tensile ($\lambda_z \geq 1$) axial loads produce different effects on the bending deformation (Fig. 6). A compressive loading has a similar effect as a voltage $\overline{V}$ on the bending: when the slab is bent slightly, every circumferential element in the sector is stretched (Fig. 7b); as the bending angle φ increases to a sufficiently large value, the inner part of the sector contracts circumferentially, and the outer part is stretched (Fig. 7c). Conversely, for a pre-stretched, slightly bent slab, every circumferential
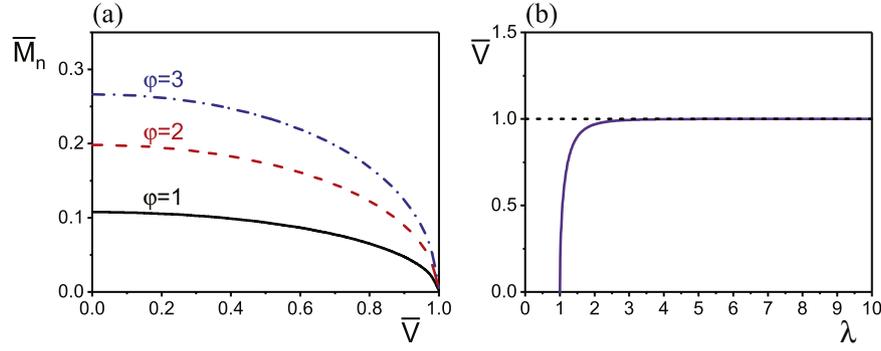
Fig. 5. (a) Plots of $\overline{M}_n - \overline{V}$ for several specific bending angles $\varphi = 1, 2, 3$ of a dielectric slab which is three times wider than thick, and no axial compression ($\lambda_z = 1, A/H = 3$); (b) Nonlinear response of a dielectric slab subject to a voltage.
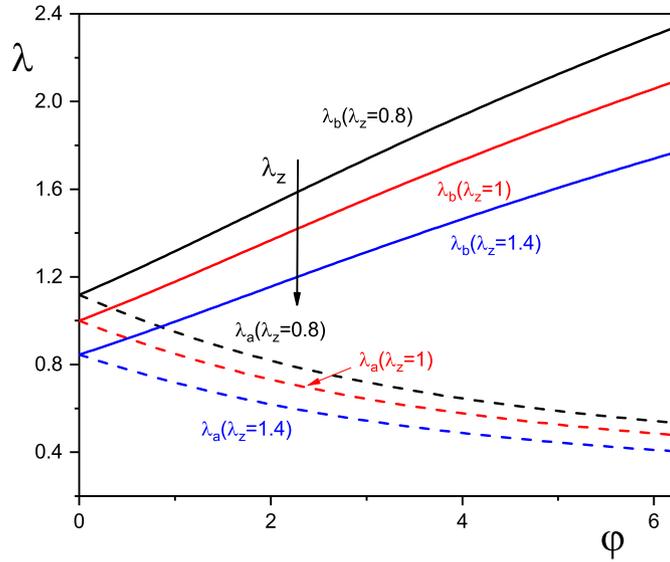
Fig. 6. Plots of $\lambda_a, \lambda_b - \varphi$ for fixed axial compressions $\lambda_z = 0.8, 1, 1.4$ of dielectric slabs with $\overline{V} = 0, A/H = 3$.

element of the solid is contracted (Fig. 8b); then as φ increases, λ_b increases, and eventually, the outer part of the solid will be stretched again for a sufficiently large φ (Fig. 8c). Notice that in both cases, the distribution of circumference stress $\overline{\tau}_{\theta\theta}$ depends almost linearly on $\overline{r}$. We can see from Fig. 9 that stretching the slab makes the solid easier to be bent.

4.2. Stability analysis

The corresponding material parameters are obtained by substituting Eq. (73) into Eqs. (A.1)–(A.3) as

$$A_{01111} = A_{01212} = A_{01313} = \mu\lambda^{-2}\lambda_z^{-2} + D_r^2, \qquad\qquad A_{02121} = A_{02222} = A_{02323} = \mu\lambda^{-2},$$

$$A_{03131} = A_{03232} = A_{03333} = \mu\lambda_z^{-2}, \qquad\qquad\qquad \Gamma_{0111} = 2\Gamma_{0122} = 2\Gamma_{0133} = 2D_r,$$

$$K_{011} = K_{022} = K_{033} = \varepsilon^{-1}. \tag{78}$$

4.2.1. Pure elastic problem

First, we consider the purely elastic slab ($\overline{V} = 0$) under bending only ($\lambda_z = 1$), a case which has been previously investigated experimentally (Gent and Cho, 1999; Roccabianca et al., 2010) and theoretically (Triantafyllidis, 1980; Destrade et al., 2009a,b; Roccabianca et al., 2010). Fig. 10 exhibits numerical results for the bending instability for different axial mode numbers $m = 0 - 5$ of elastic slabs with $A/H = 1, 3$ and 4, and $L/H = 10$, respectively. The solid buckles when the stretch of the inner surface λ_a reaches the highest point of the $\lambda_c - q$ curve. We find that the bending instability occurs with decreasing critical stretch λ_c as m increases and the buckling mode with $m = 0$ always occurs first, indicating that only circumferential wrinkles occur at the onset of instability. For instance, a slab with $A/H = 1, 3, 4$ buckles in modes $q = 2, 7, 10$ and $m = 0$ when the circumferential stretch of the inner surface of the sector reaches $\lambda_c = 0.56091, 0.5614, 0.56135$ and the bending angle reaches $\varphi_c = 1.43, 4.23, 5.72$, respectively. Notice that the perturbation decays dramatically along the radius, and that the displacement on the inner face is several orders of magnitude larger than that on the outer face.

Fig. 11 reports the critical number of circumferential wrinkles q, the critical stretch λ_c and the critical bending angle φ_c as functions of the aspect ratio A/H. For a given A/H, each mode number q corresponds a different value of the critical stretch λ_c and a series of branches can be obtained by taking $q = 1, 2, 3, \ldots$ However only the highest value is meaningful, thus the other curves below the highest curve are
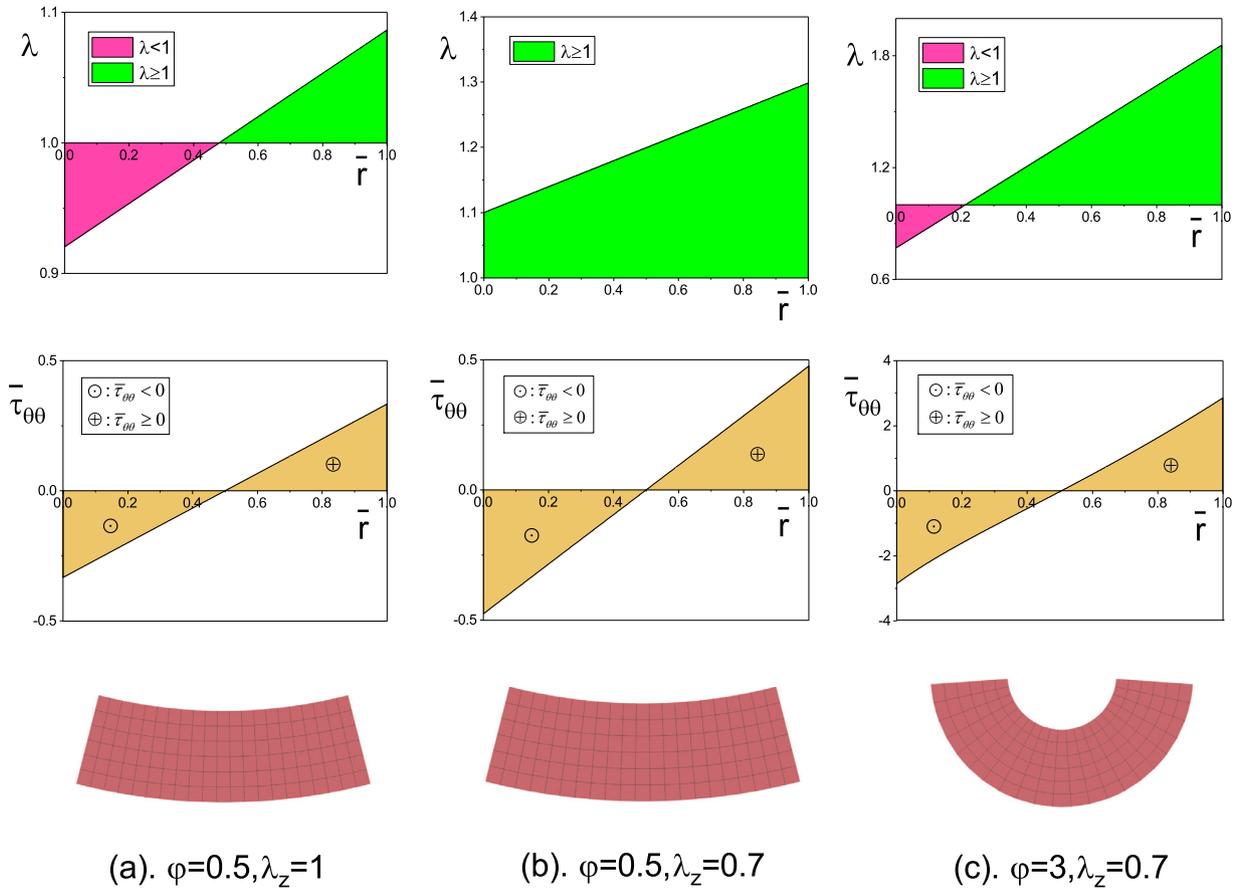
Fig. 7. Purely elastic bending of a dielectric slab which is three times wider than thick ($\overline{V} = 0, A/H = 3$) for various bending angles and axial compression ratios: (a) $\varphi = 0.5, \lambda_z = 1$; (b) $\varphi = 0.5, \lambda_z = 0.7$; (c) $\varphi = 3, \lambda_z = 0.7$. The top, middle and bottom rows show the variations through the thickness of the circumferential stretch and of the stress distributions, and the resulting bending shapes, respectively.

not presented in the $\lambda_c - A/H$ plot. We observe that as A/H increases, the mode number q increases, indicating that more wrinkles appear as instability occurs for a more slender slab. The critical bending angle φ_c increases linearly as A/H increases. For a slab with sufficiently large width aspect ratio $A/H(> 4.46)$, the structure can be bent into a tube without encountering any instability (Fig. 11b). In the half-space limit ($A/H \to 0$), the critical stretch is $\lambda_c = 0.5437$, which corresponds to the threshold value of surface instability of a compressed elastic slab (Biot, 1965; Destrade et al., 2009b). When A/H is small, the critical stretch λ_c varies significantly as A/H varies. While for a slab with sufficiently large A/H, λ_c reaches a horizontal asymptote $\lambda_c \approx 0.5618$.

4.2.2. Effect of the voltage

We now consider the effect of the applied voltage $\overline{V}$ on the bending instability of a dielectric slab. Fig. 12 presents plots of λ_c versus q for a range of modes $m = 0 - 5$ and the corresponding wrinkling shapes when instability occurs for dielectric slabs with $A/H = 3, L/H = 1.5$ and subject to $\overline{V} = 0, 0.2, 0.4, 0.6, 0.7, 0.76$. Here we fix the axial deformation of the bending deformation as a 15% contraction ($\lambda_z = 0.85$). For each of the cases (a)–(f) shown in Fig. 12, the buckling mode is $(m, q) = (0, 7), (0, 8), (1, 1), (1, 1), (1, 0)$ and $(1,0)$, respectively. The critical stretch λ_c increases as $\overline{V}$ increases. For the cases where the applied voltage is small, only circumferential wrinkles occur ($m = 0, q \neq 0$) when bending buckling happens, and the mode number q increases as the voltage increases (Fig. 12a and b). As the voltage increases further, both circumferential and axial wrinkles occur simultaneously ($m \neq 0, q \neq 0$) at the onset of bending instability (Fig. 12c and d) and combine to give a 2D pattern. Finally, for dielectric slabs subject to sufficiently large voltage, a slight bending will drive the instability of the structure and in this case, only axial wrinkling occurs (($m \neq 0, q = 0$), see Fig. 12e and f). It should be mentioned that the maximal number of axial wrinkles is one ($m = 0, 1$).

We extract the critical bending angle φ_c when the instability occurs and the critical moment $\overline{M}_{nc}$ needed to drive the instability for the cases presented in Fig. 12, and plot them in Fig. 13 as the applied voltage $\overline{V}$ changes. It can be seen that both $\overline{\varphi}_c$ and $\overline{M}_{nc}$ decrease as $\overline{V}$ increases, indicating that the application of the voltage makes the dielectric slab more susceptible to fail. One may expect that $\overline{\varphi}_c$ and $\overline{M}_{nc}$ will be zero for a critical λ_{zc}, corresponding the critical value of instability of a compressed elastic slab (Dorfmann and Ogden, 2014a; Biot, 1963).

4.2.3. Effect of the axial constraint

Here, we investigate the effect of the axial compression, as measured by the axial stretch ratio λ_z, on the bending instability of dielectric slabs. Fig. 14 displays numerical results for the bending instability of dielectric slabs with $A/H = 3, L/H = 1.5$ and subject to $\overline{V} = 0.3$ and $\lambda_z = 1, 0.9, 0.8, 0.75, 0.7, 0.63$, respectively. Fig. 15 presents the corresponding φ_c and $\overline{M}_{nc}$ when buckling occurs. For each of the cases (a)-(f) shown in Fig. 14, the buckling mode is $(m, q) = (0, 9), (0, 8), (1, 1), (1, 1), (1, 0)$ and $(1,0)$, respectively. We can see that decreasing
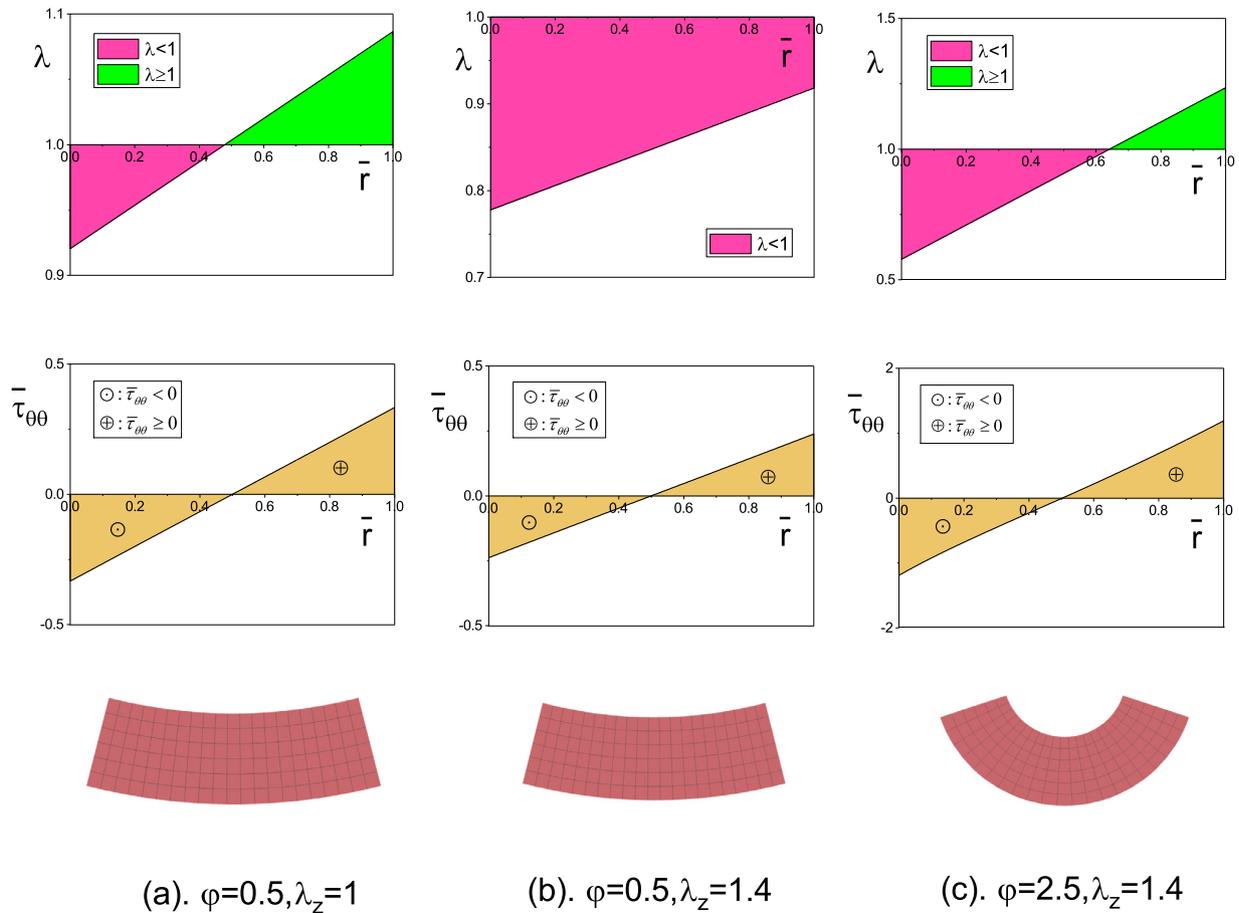
Fig. 8. Purely elastic bending of a dielectric slab which is three times wider than thick ($\overline{V} = 0, A/H = 3$) for various bending angles and axial elongation ratios: (a) $\overline{\varphi} = 0.5, \lambda_z = 1$; (b) $\overline{\varphi} = 0.5, \lambda_z = 1.4$; (c) $\overline{\varphi} = 2.5, \lambda_z = 1.4$. The top, middle and bottom rows show the variations through the thickness of the circumferential stretch and of the stress distributions, and the resulting bending shapes, respectively.
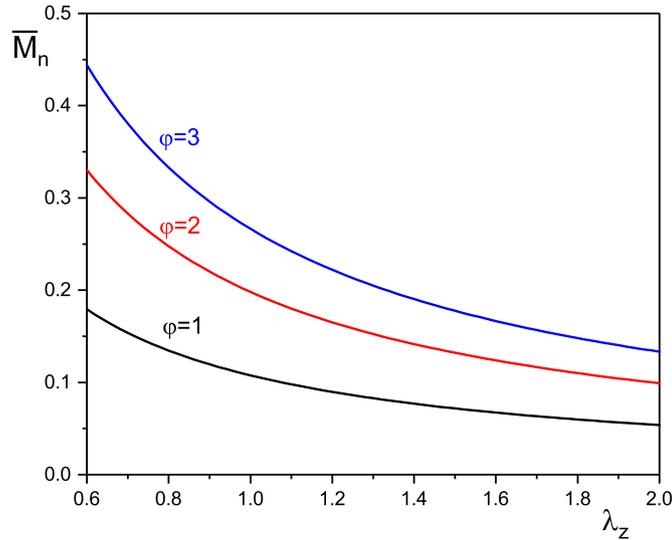
Fig. 9. Plots of $\overline{M}_n - \lambda_z$ for bending angle $\varphi = 1, 2, 3$ of a dielectric slab with $\overline{V} = 0, A/H = 3$.

the axial stretch ratio has a similar effect as increasing the applied voltage $\overline{V}$ on the bending buckling behavior of dielectric slabs, i.e., the critical stretch λ_c increases as λ_z decreases, and circumferential wrinkles occur first and eventually only axial wrinkles exist as λ_z decreases to a sufficiently small value. Note that when the axial compression is small, the mode number q decreases as λ_z increases (Fig. 14a and b), which is different from the case of increasing $\overline{V}$ (Fig. 12a and b). Due to the competition mechanisms of the effects of $\overline{V}$ and λ_z on the bending instability of the structure, the $\varphi_c, \overline{M}_{nc} - \lambda_z$ curves are non-monotone. On the one hand, decreasing λ_z increases the thickness of the slab and thus decreases the true electric field, which consequently increases the stability of the structure. On the
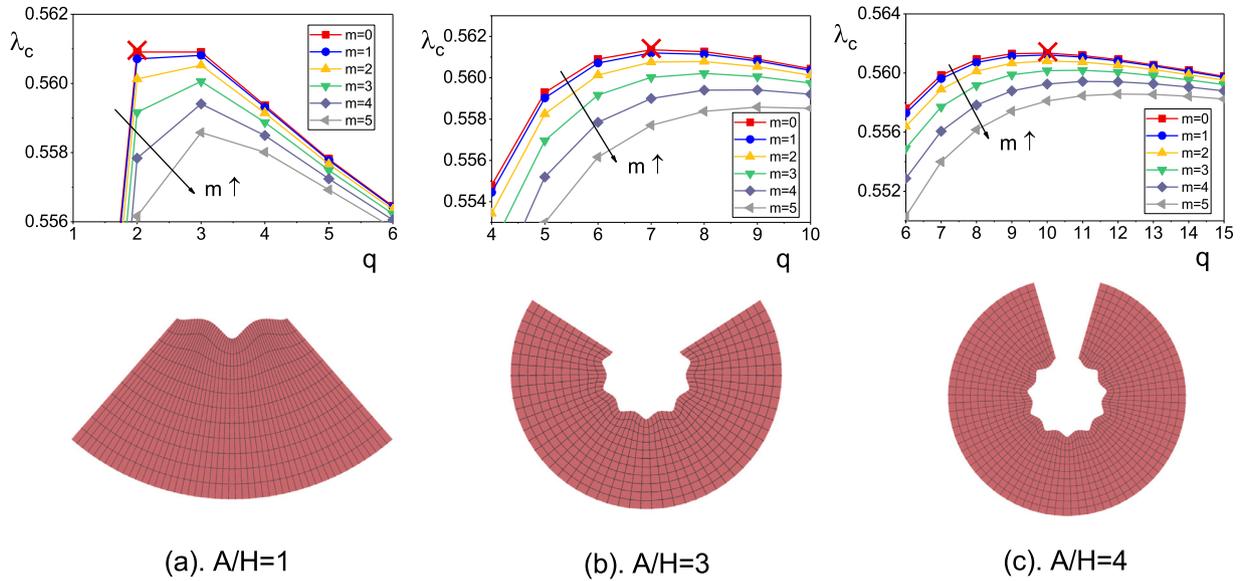
Fig. 10. Elastic bending instability of a dielectric slab with fixed axial compression ($\overline{V} = 0, \lambda_z = 1$) for various width aspect ratios: (a) $A/H = 1$; (b) $A/H = 3$; (c) $A/H = 4$ and fixed length aspect ratio $L/H = 10$. The top row shows plots of the critical circumferential stretch λ_c versus the number of circumferential wrinkles q for a range of axial modes $m = 0 - 5$. The bottom row shows the corresponding wrinkling shapes when instability occurs. The highest point of $\lambda_c - q$ curves for each ease is marked by cross, representing the onset of the instability. In this case the $m = 0$ plot is always on top and there are no axial wrinkles, only circumferential.
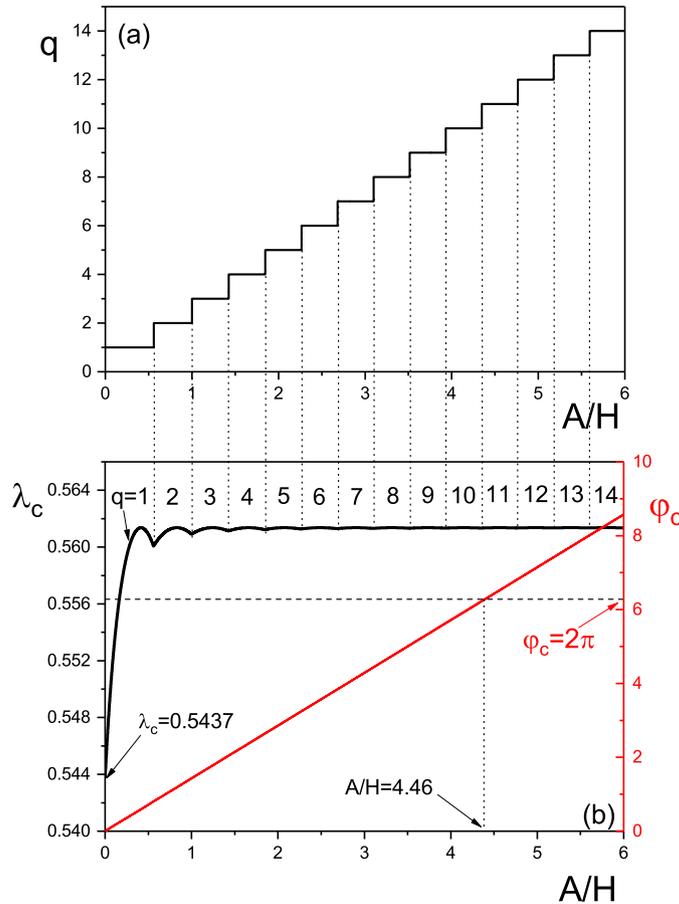
Fig. 11. (a) Critical circumferential mode number q and (b) stretch λ_c (evaluated at the inner face of the bent sector r_a) and critical bending angle φ_c versus width aspect ratio A/H of an elastic slab ($\overline{V} = 0$) under bending only ($\lambda_z = 1$) at the onset of buckling.

(a). $\overline{V}=0$

(b). $\overline{V}=0.2$

(c). $\overline{V}=0.4$
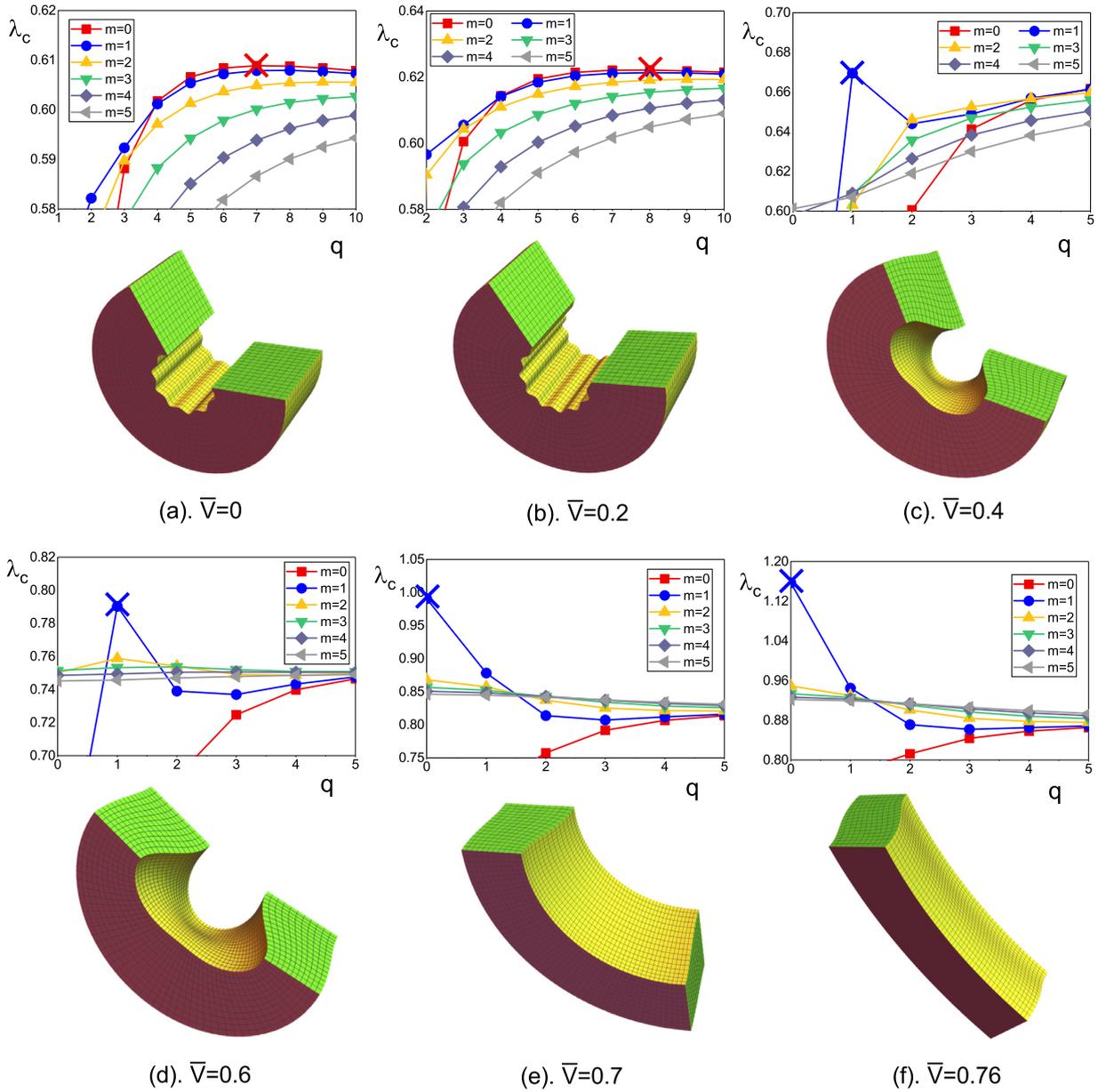
(d). $\overline{V}=0.6$

(e). $\overline{V}=0.7$

(f). $\overline{V}=0.76$

Fig. 12. Bending instability of compressed dielectric slabs which are 3 times wider and 1.5 times taller than thick ($A/H = 3, L/H = 1.5, \lambda_z = 0.85$) and subject to increasing voltages: (a) $\overline{V} = 0$; (b) $\overline{V} = 0.2$; (c) $\overline{V} = 0.4$; (d) $\overline{V} = 0.6$; (e) $\overline{V} = 0.7$; (f) $\overline{V} = 0.76$. The top rows are plots of λ_c versus q for a range of modes $m = 0 - 5$ and bottom rows are the corresponding wrinkling shapes when instability occurs. In cases (a) and (b), circumferential wrinkles occurs and in cases (e) and (f), axial wrinkles occurs whereas in cases (c) and (d), a two-dimensional (circumferential and axial) pattern emerges.
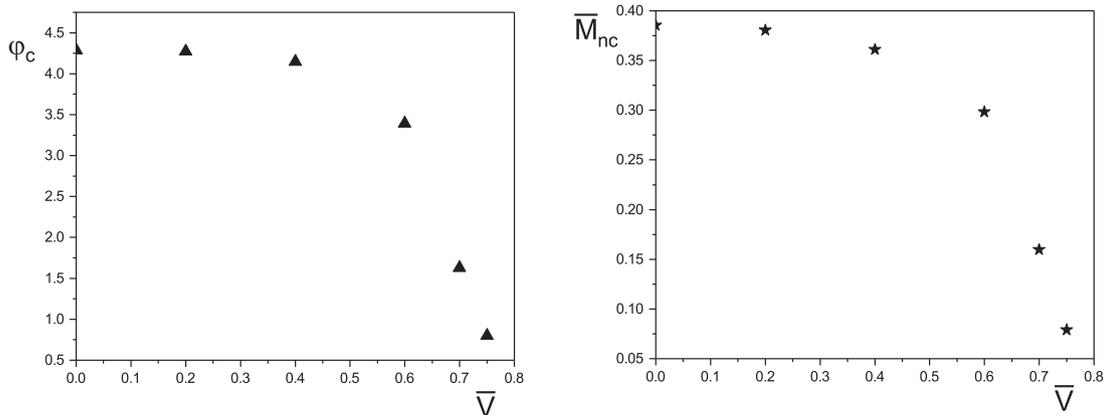
Fig. 13. Effect of the applied voltage $\overline{V}$ on the critical values of bending angle φ_c and moment $\overline{M}_{nc}$ for dielectric slabs with $A/H = 3, L/H = 1.5, \lambda_z = 0.85$.
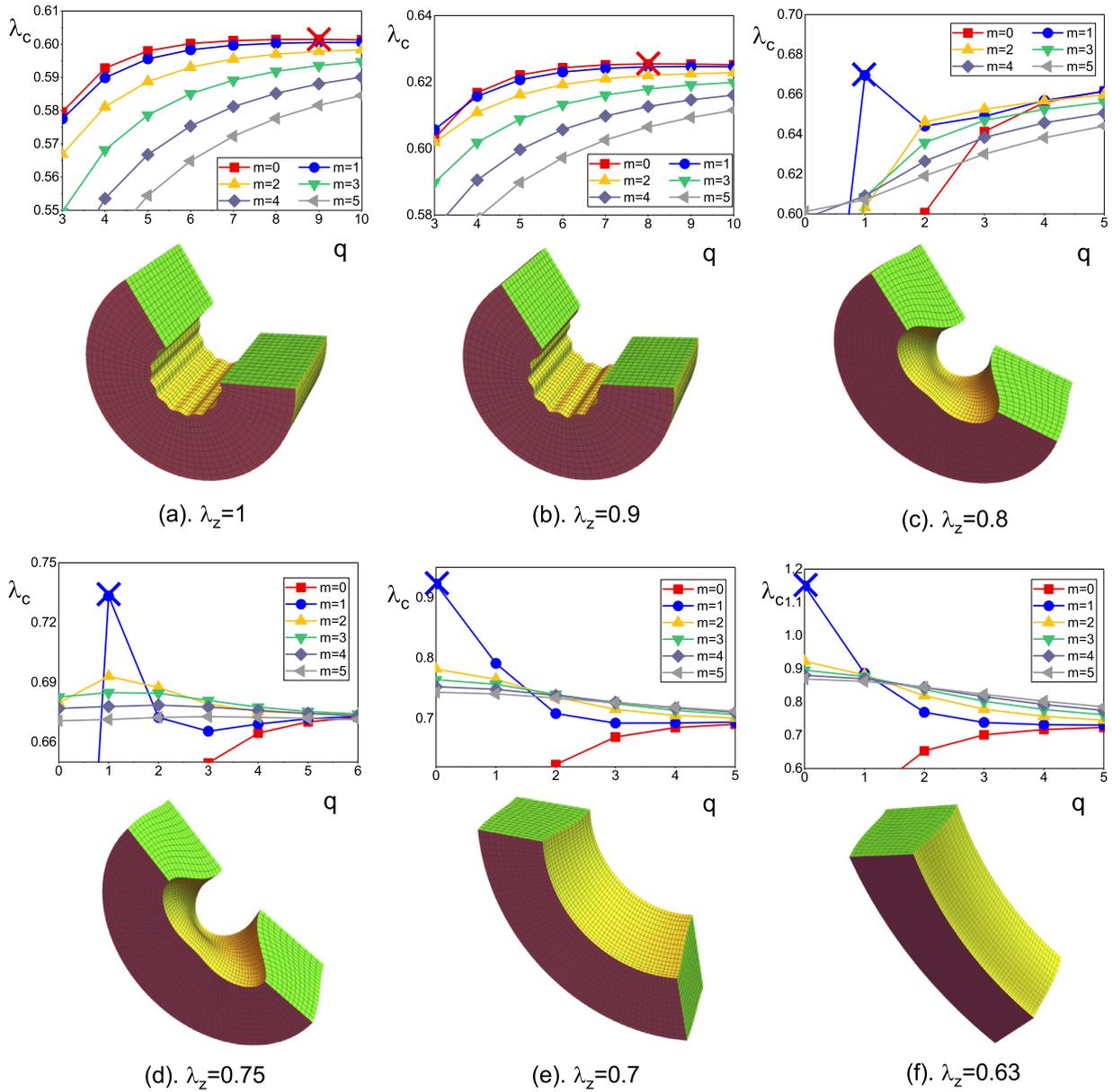
Fig. 14. Bending instability of dielectric slabs with $A/H = 3, L/H = 1.5, \overline{V} = 0.3$ and subject to (a) $\lambda_z = 1$; (b) $\lambda_z = 0.9$; (c) $\lambda_z = 0.8$; (d) $\lambda_z = 0.75$; (e) $\lambda_z = 0.7$; (f) $\lambda_z = 0.63$. The top rows are plots of λ_c versus q for a range of modes $m = 0 - 5$ and bottom rows are the corresponding wrinkling shapes when instability occurs. In cases (a) and (b), circumferential wrinkles occurs and in cases (e) and (f), axial wrinkles occurs whereas in cases (c) and (d), a two dimensional (circumferential and axial) pattern emerges.
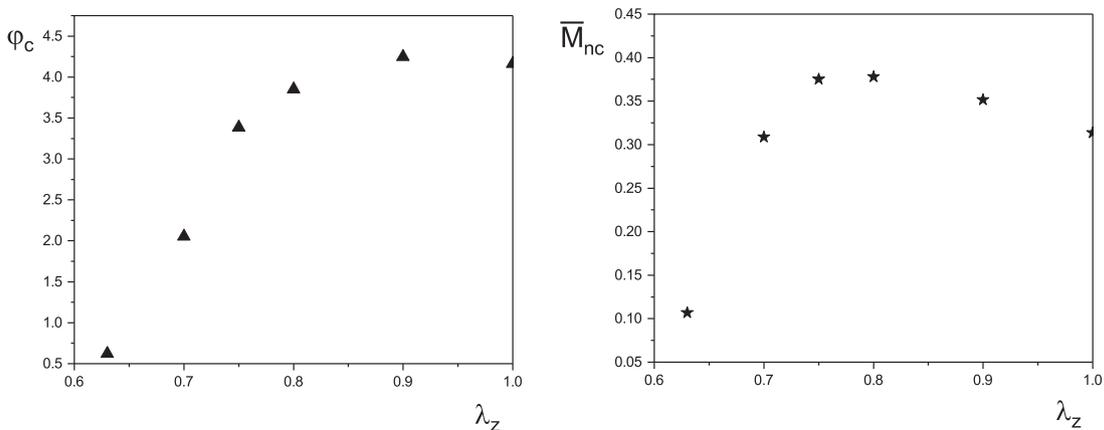
Fig. 15. Effect of the axial compression, as measured by the axial stretch ratio λ_z, on the critical values of bending angle φ_c and moment $\overline{M}_{nc}$ for dielectric slabs with $A/H = 3, L/H = 1.5, \overline{V} = 0.3$.

other hand, decreasing λ_z makes the structure easier to fail in the axial direction and has a destabilizing influence on the slab. As a result, φ_c and $\overline{M}_{nc}$ increase first and then decrease to zero, as λ_z decreases (Fig. 15), indicating that the voltage $\overline{V}$ plays a major role when the structure is only slightly compressed, while the axial compression λ_z presents the dominant influence when the structure is dramatically compressed.

5. Conclusions

We presented a theoretical analysis of the finite bending deformation and the associated bending instability of an incompressible dielectric slab subject to a combined action of voltage and mechanical moments. We derived the three-dimensional equations governing the static finite bending deformation and the associated incremental deformation of the slab for a general form of energy function. In particular, we studied explicit expressions of the radially inhomogeneous biasing fields in the slab for ideal neo-Hookean dielectric materials. We took the electric loading to be voltage-controlled and so we chose a state vector accordingly to rewrite the incremental governing equation in the Stroh differential form. We used the surface impedance matrix method to obtain numerically the bending threshold for the onset of the instability and the wrinkled shape of the shell when bending instability occurs.

We first studied the effects of the applied voltage and axial compression on the finite bending deformation. We showed that the length aspect ratios of the slab L/H does not affect the bending deformation of the slab. The applied voltage increases the circumferential stretch in the body so that every circumferential element in a slightly bent slab is stretched. The moments needed to drive the specific bending of the slab decrease as the voltage increases, indicating that the application of the voltage makes the slab easier to bend. We found that the compressive axial constraint has a similar effect as the applied voltage, while on the contrary, every circumferential element in a slightly bent slab, subject to axial pre-stretch, is contracted. As the axial stretch increases, the moments needed to drive a specific bending of the slab decrease, indicating that the axial pre-stretch makes the slab easier to bend. In any case, the circumferential stretch deforms linearly along the radial direction and the transverse stress of the inner part of the sector is always compressive while that of the outer part is always tensile.

We then investigated the combined influences of the applied voltage and axial constraint on the instability of a dielectric slab. We obtained the critical circumferential stretch on the inner surface of the deformed shell, as well as the wrinkled shape when the bending instability occurs. We recovered the results of the purely elastic problem to validate our analysis. Theoretically, the application of the voltage and the axial constraint both play a destabilizing effect, i.e., make the slab more susceptible to wrinkling instability. The two effects compete with each other, and an increase in the axial compressive loads leads to a decrease in the true electric field in the body. The applied voltage plays the main role when the constraint is small, while the constraint becomes dominant when the compression is sufficiently large.

In this article we focused on the formation of small-amplitude wrinkles in a bent and axially compressed dielectric slab. We did not look at post-buckling behavior or if creases might have preceded wrinkles. This is certainly the case in the *in-plane compression of an elastic half-space*, where creases form much earlier ($\lambda_c = 0.65$) than the wrinkles predicted by the linearised buckling analysis of Biot ($\lambda_c = 0.54$), i.e. with more than 10% strain difference (Hong et al., 2009). However, recent Finite Element simulations show that in *bending*, creases occur only a few percent of strain earlier than wrinkles, and that their number and wavelength can be predicted by the linearized analysis (Sigaeva et al., 2018). Hence we argue that our analysis is justified as a good approximation for predicting the onset and wavelength of buckling, although of course a fully multi-physics Finite Element Analysis is required to settle this question.

Moreover, wrinkles have indeed been observed in loaded dielectric elastomers with free sides (e.g. Plante and Dubowsky, 2006; Liu et al., 2016).

To create creases in a dielectric membrane, one could glue one side of a slab to a rigid, conducting substrate, as done by Wang and Zhao (2013), but the corresponding boundary value problem is then different from the one studied here, where both sides were free of traction.

Acknowledgments

Appendix A. Non-zero electro-elastic moduli

Here we use the incremental theory of electro-elasticity to compute the non-zero components of the instantaneous electro-elastic moduli with respect to the specific deformation gradient (17), as follows (Wu et al., 2017; Dorfmann and Ogden, 2010a)

$$
\begin{aligned}
A_{01111} =& 2\lambda^{-4}\lambda_z^{-4}\Big\{\lambda^4\big[2\Omega_{22}+\lambda_z^2\big(\Omega_2+4\Omega_{25}D_r^2\big)+\lambda_z^4 D_r^2\big(\Omega_5+2\Omega_{55}D_r^2\big)\big]\\
&+2\big[\Omega_{11}+\lambda_z^4\Omega_{22}+2\lambda_z^2\big(\Omega_{12}+2\Omega_{26}D_r^2\big)+4D_r^2\big(\Omega_{16}+\Omega_{66}D_r^2\big)\big]\\
&+\lambda^2\lambda_z^4\big(\Omega_2+4\Omega_{25}D_r^2\big)+4\lambda^2\big(\Omega_{12}+2\Omega_{26}D_r^2\big)\\
&+\lambda^2\lambda_z^2\big[\Omega_1+4\Omega_{22}+8\Omega_{56}D_r^4+D_r^2(4\Omega_{15}+6\Omega_6)\big]\Big\},\\
A_{01122} =& 4\lambda^{-2}\lambda_z^{-4}\Big\{\Omega_{12}+\lambda_z^2\Omega_{22}+\lambda^4\lambda_z^2\big[\Omega_{12}+\lambda_z^2\Omega_{22}+\lambda_z^2 D_r^2\big(\Omega_{15}+\lambda_z^2\Omega_{25}\big)\big]+2\Omega_{26}D_r^2\\
&+\lambda^2\big[\Omega_{22}+\lambda_z^6\Omega_{22}+\lambda_z^2\Omega_{11}+\lambda_z^2\Omega_2+\lambda_z^2 D_r^2(2\Omega_{16}+\Omega_{25})+2\lambda_z^4\big(\Omega_{12}+\Omega_{26}D_r^2\big)\big]\Big\},\\
A_{01133} =& 4\lambda^{-4}\lambda_z^{-2}\Big\{\Omega_{12}+\lambda^2\Omega_{22}+\lambda^2\lambda_z^4\big[\Omega_{12}+\lambda^2\Omega_{22}+\lambda^2 D_r^2\big(\Omega_{15}+\lambda^2\Omega_{25}\big)\big]+2\Omega_{26}D_r^2\\
&+\lambda_z^2\big[\Omega_{22}+\lambda^6\Omega_{22}+\lambda^2\Omega_{11}+\lambda^2\Omega_2+\lambda^2 D_r^2(2\Omega_{16}+\Omega_{25})+2\lambda^4\big(\Omega_{12}+\Omega_{26}D_r^2\big)\big]\Big\},
\end{aligned}
$$

$$A_{01212} = 2\lambda^{-2}\lambda_z^{-2}\{\Omega_1 + 2\Omega_6 D_r^2 + \lambda_z^2[\Omega_2 + \lambda^2 D_r^2(\Omega_5 + \lambda^2\Omega_6)]\},$$

$$A_{01313} = 2\lambda^{-2}\lambda_z^{-2}\{\Omega_1 + 2\Omega_6 D_r^2 + \lambda^2[\Omega_2 + \lambda_z^2 D_r^2(\Omega_5 + \lambda_z^2\Omega_6)]\},$$

$$A_{01221} = -2\lambda_z^{-2}\Omega_2 + 2\lambda^2\Omega_6 D_r^2, \quad A_{01331} = -2\lambda^{-2}\Omega_2 + 2\lambda_z^2\Omega_6 D_r^2,$$

$$A_{02121} = 2\lambda^2(\Omega_1 + \lambda_z^2\Omega_2 + \Omega_6 D_r^2), \quad A_{03131} = 2\lambda_z^2(\Omega_1 + \lambda^2\Omega_2 + \Omega_6 D_r^2),$$

$$A_{02222} = 2\lambda_z^{-4}[\lambda_z^2\Omega_2 + 2\Omega_{22} + \lambda^2(\lambda_z^4\Omega_1 + 4\lambda_z^4\Omega_{12} + \lambda_z^6\Omega_2 + 4\lambda_z^4\Omega_{22})$$
$$+2\lambda^4\lambda_z^4(\Omega_{11} + 2\lambda_z^2\Omega_{12} + \lambda_z^4\Omega_{22})],$$

$$A_{02233} = 4\lambda^{-2}\lambda_z^{-2}[\Omega_{22} + \lambda^4\lambda_z^2(\lambda_z^4\Omega_{12} + \lambda_z^2\Omega_{11} + \lambda_z^2\Omega_2 + \Omega_{22})$$
$$+\lambda^6\lambda_z^4(\Omega_{12} + \lambda_z^2\Omega_{22}) + \lambda^2(2\lambda_z^2\Omega_{12} + \lambda_z^4\Omega_{22})],$$

$$A_{02323} = 2\lambda^2\Omega_1 + 2\lambda_z^{-2}\Omega_2, \quad A_{02332} = -2\lambda^2\lambda_z^2\Omega_2, \quad A_{03232} = 2\lambda_z^2\Omega_1 + \lambda^{-2}\Omega_2,$$

$$A_{03333} = 2\lambda^{-4}[\lambda^2\Omega_2 + 2\Omega_{22} + \lambda_z^2(\lambda^4\Omega_1 + 4\lambda^4\Omega_{12} + \lambda^6\Omega_2 + 4\lambda^4\Omega_{22})$$
$$+2\lambda^4\lambda_z^4(\Omega_{11} + 2\lambda^2\Omega_{12} + \lambda^4\Omega_{22})], \tag{A.1}$$

$$\Gamma_{0111} = 4\lambda^{-4}\lambda_z^{-4}D_r\{\Omega_{16} + \lambda_z^2\Omega_{26} + \lambda^6\lambda_z^4(\Omega_{24} + \lambda_z^2\Omega_{45}D_r^2)$$
$$+\lambda^4\lambda_z^z[\lambda_z^4\Omega_{24} + \Omega_{25} + \lambda_z^2(\Omega_{14} + \Omega_5 + 2\Omega_{46}D_r^2 + \Omega_{55}D_r^2)]$$
$$+2\Omega_{66}D_r^2 + \lambda^2[\lambda_z^4\Omega_{25} + \Omega_{26} + \lambda_z^2(\Omega_{15} + 3\Omega_{56}D_r^2 + 2\Omega_6)]\},$$

$$\Gamma_{0122} = 2\lambda^{-2}\lambda_z^{-2}D_r[\lambda^2\lambda_z^2\Omega_5 + (1 + \lambda^4\lambda_z^2)\Omega_6],$$

$$\Gamma_{0133} = 2\lambda^{-2}\lambda_z^{-2}D_r[\lambda^2\lambda_z^2\Omega_5 + (1 + \lambda^2\lambda_z^4)\Omega_6],$$

$$\Gamma_{0221} = 4\lambda^{-2}\lambda_z^{-4}D_r[\lambda^6\lambda_z^6(\Omega_{14} + \lambda_z^2\Omega_{24}) + \lambda^4\lambda_z^4(\Omega_{15} + \Omega_{24} + \lambda_z^2\Omega_{25})$$
$$+\Omega_{26} + \lambda^2\lambda_z^2(\Omega_{16} + \Omega_{25} + \lambda_z^2\Omega_{26})],$$

$$\Gamma_{0331} = 4\lambda^{-4}\lambda_z^{-2}D_r[\lambda^6\lambda_z^6(\Omega_{14} + \lambda^2\Omega_{24}) + \lambda^4\lambda_z^4(\Omega_{15} + \Omega_{24} + \lambda^2\Omega_{25})$$
$$+\Omega_{26} + \lambda^2\lambda_z^2(\Omega_{16} + \Omega_{25} + \lambda^2\Omega_{26})], \tag{A.2}$$

$$K_{011} = \lambda^{-4}\lambda_z^{-4}[2\lambda^2\lambda_z^2(\lambda^2\lambda_z^2\Omega_5 + \Omega_6 + \lambda^4\lambda_z^4\Omega_4)$$
$$+4D_r^2(\lambda^8\lambda_z^8\Omega_{44} + 2\lambda^6\lambda_z^6\Omega_{45} + 2\lambda^4\lambda_z^4\Omega_{46} + \lambda^4\lambda_z^4\Omega_{55} + 2\lambda^2\lambda_z^2\Omega_{56} + \Omega_{66})],$$

$$K_{022} = 2(\Omega_5 + \lambda^2\Omega_6 + \lambda^{-2}\Omega_4), \quad K_{033} = 2(\Omega_5 + \lambda_z^2\Omega_6 + \lambda_z^{-2}\Omega_4). \tag{A.3}$$

Appendix B. Derivation of the Stroh formulation

First, rewriting Eq. (40) by using solutions (47) gives

$$U_r' = -\frac{1}{r}(U_r + nU_\theta + krU_z). \tag{B.1}$$

Next, eliminating $\dot{D}_{l0\theta}$ from Eqs. (42)$_4$ and using (43)$_2$ and utilizing Eq. (47), yields

$$U_\theta' = \frac{1}{r}\left[\frac{n(\gamma_{12} - \tau_{rr})}{\gamma_{12}}U_r + \frac{\gamma_{12} - \tau_{rr}}{\gamma_{12}}U_\theta + \frac{1}{\gamma_{12}}(r\Sigma_{r\theta}) - \frac{n}{\gamma_{12}}\frac{\Gamma_{0122}}{K_{022}}\Phi\right]. \tag{B.2}$$

Similarly, eliminating $\dot{D}_{l0z}$ from Eqs. (42)$_5$ and using (43)$_3$ and utilizing Eq. (47), yields

$$U_z' = \frac{1}{r}\left[\frac{kr(\gamma_{13} - \tau_{rr})}{\gamma_{13}}U_r + \frac{1}{\gamma_{13}}(r\Sigma_{rz}) - \frac{kr}{\gamma_{13}}\frac{\Gamma_{0133}}{K_{033}}\Phi\right]. \tag{B.3}$$

Next, we substitute Eqs. (43)$_{2,3}$ and (47) into Eq. (45) and using Eqs. (B.2) and (B.3) to get the expression for $(r\Delta_r)'$, as follows

$$(r\Delta_r)' = \frac{1}{r}\left[\xi_1 U_r - \frac{n\tau_{rr}}{\gamma_{12}}\frac{\Gamma_{0122}}{K_{022}}U_\theta + \frac{n}{\gamma_{12}}\frac{\Gamma_{0122}}{K_{022}}(r\Sigma_{r\theta}) + \frac{kr}{\gamma_{13}}\frac{\Gamma_{0133}}{K_{033}}(r\Sigma_{rz}) + \xi_2\Phi\right]. \tag{B.4}$$

These are the first four lines of the Stroh formulation.

Substituting Eqs. (42)$_{1,2,6,8}$, (43)$_{2,3}$ and (47) into Eq. (44)$_1$ and using Eqs. (B.1)–(B.3) results in

$$(r\Sigma_{rr})' = \frac{1}{r}[\kappa_{11t}U_r + \kappa_{12}U_\theta + \kappa_{13}U_z - (\Gamma_{0111} - \Gamma_{0221})r\Delta_r + r\Sigma_{rr}$$
$$-\frac{n(\gamma_{12} - \tau_{rr})}{\gamma_{12}}r\Sigma_{r\theta} - \frac{kr(\gamma_{13} - \tau_{rr})}{\gamma_{13}}r\Sigma_{rz} + \xi_1\Phi]. \tag{B.5}$$

Similarly, substituting Eqs. (42)$_{1, 2, 4, 6, 9}$, (43)$_2$ and (47) into Eq. (44)$_2$ and using Eqs. (B.1) and (B.2) gives

$$(r\Sigma_{r\theta})' = \frac{1}{r}[\kappa_{12}U_r + \kappa_{22}U_\theta + \kappa_{23}U_z - n(\Gamma_{0111} - \Gamma_{0221})r\Delta_r$$

$$+n(r\Sigma_{rr}) - \frac{\gamma_{12} - \tau_{rr}}{\gamma_{12}}r\Sigma_{r\theta} - \frac{n\tau_{rr}}{\gamma_{12}}\frac{\Gamma_{0122}}{K_{022}}\Phi]. \qquad (B.6)$$

Then substituting Eqs. (42)$_{1, 3, 7}$ and (47) into Eq. (44)$_3$ and using Eq. (B.1), we obtain

$$(r\Sigma_{rz})' = \frac{1}{r}[\kappa_{13}U_r + \kappa_{23}U_\theta + \kappa_{33}U_z - kr(\Gamma_{0111} - \Gamma_{0331})r\Delta_r$$

$$+kr(r\Sigma_{rr})]. \qquad (B.7)$$

Finally, from Eqs. (43)$_1$ and (47) and using Eq. (B.1), we have

$$\Phi' = \frac{1}{r}[(\Gamma_{0111} - \Gamma_{0221})U_r + n(\Gamma_{0111} - \Gamma_{0221})U_\theta$$

$$+kr(\Gamma_{0111} - \Gamma_{0331})U_z - K_{011}r\Delta_r]. \qquad (B.8)$$

Now we can write Eqs. (B.1)–(B.8) in the Stroh matrix form, as presented in Eq. (49).

References

Balbi, V., Kuhl, E., Ciarletta, P., 2015. Morphoelastic control of gastro-intestinal organogenesis: theoretical predictions and numerical insights. J. Mech. Phys. Solids 78, 493–510.

Bar-Cohen, Y., 2002. Electro-active polymers: current capabilities and challenges. In: Bar-Cohen, Y. (Ed.), Proceedings of the 4th Electroactive Polymer Actuators and Devices (EAPAD) Conference, 9th Smart Structures and Materials Symposium. SPIE Publishers, San Diego. Bellingham, WA, pp. 1–7.

Bar-Cohen, Y., 2004. Electroactive Polymer (EAP) Actuators as Artificial Muscles: Reality, Potential, and Challenges, 136. SPIE press.

Biot, M.A., 1963. Exact theory of buckling of a thick slab. Appl. Sci. Res. A 12 (2), 183–198.

Biot, M.A., 1965. Mechanics of Incremental Deformations. John Wiley, New York.

Bortot, E., 2017. Analysis of multilayer electro-active spherical balloons. J. Mech. Phys. Solids 101, 250–267.

Bortot, E., 2018. Analysis of multilayer electro-active tubes under different constraints.ArXiv preprint arXiv:1801.10102.

Brochu, P., Pei, Q.B., 2010. Advances in dielectric elastomers for actuators and artificial muscles. Macromol. Rapid Commun. 31 (1), 10–36.

Destrade, M., Gilchrist, M.D., Motherway, J.A., Murphy, J.G., 2009a. Bimodular rubber buckles early in bending. Mech. Mater. 42, 469–476.

Destrade, M., Ní Annaidh, A., Coman, C.D., 2009b. Bending instabilities of soft biological tissues. Int. J. Solids Struct. 46 (25–26), 4322–4330.

Destrade, M., Ogden, R.W., Sgura, I., Vergori, L., 2014. Straightening wrinkles. J. Mech. Phys. Solids 65, 1–11.

Dorfmann, A., Ogden, R.W., 2005. Nonlinear electroelasticity. Acta Mech. 174 (3–4), 167–183.

Dorfmann, A., Ogden, R.W., 2006. Nonlinear electroelastic deformations. J. Elasticity 82 (2), 99–127.

Dorfmann, A., Ogden, R.W., 2010a. Electroelastic waves in a finitely deformed electroactive material. IMA J. Appl. Math. 75 (4), 603–636.

Dorfmann, A., Ogden, R.W., 2010b. Nonlinear electroelastostatics: incremental equations and stability. Int. J. Eng. Sci. 48 (1), 1–14.

Dorfmann, L., Ogden, R.W., 2014a. Instabilities of an electroelastic plate. Int. J. Eng. Sci. 77, 79–101.

Dorfmann, L., Ogden, R.W., 2014b. Nonlinear response of an electroelastic spherical shell. Int. J. Eng. Sci. 85, 163–174.

Dorfmann, L., Ogden, R.W., 2016. Nonlinear Theory of Electroelastic and Magnetoelastic Interactions. Springer, New York.

Ericksen, J.L., 2007. Theory of elastic dielectrics revisited. Arch. Ration. Mech. An. 183 (2), 299–313.

Galich, P.I., Rudykh, S., 2017. Shear wave propagation and band gaps in finitely deformed dielectric elastomer laminates: long wave estimates and exact solution. J. Appl. Mech. 84, 091002.

Gent, A.N., Cho, I.S., 1999. Surface instabilities in compressed or bent rubber blocks. Rubber Chem. Technol. 72 (2), 253–262.

Getz, R., Shmuel, G., 2017. Band gap tunability in deformable dielectric composite plates. Int. J. Solids Struct. 128, 11–22.

Green, A.E., Zerna, W., 1954. Theoretical Elasticity. University Press, Oxford. Reprinted by Dover, New York

He, L.W., Lou, J., Du, J.K., Wang, J., 2017. Finite bending of a dielectric elastomer actuator and pre-stretch effects. Int. J. Mech. Sci. 122, 120–128.

Hong, W., Zhao, X.H., Suo, Z.G., 2009. Formation of creases on the surfaces of elastomers and gels. Appl. Phys. Lett. 95, 111901.

Keplinger, C., Kaltenbrunner, M., Arnold, N., Bauer, S., 2010. Röntgen's electrode-free elastomer actuators without electromechanical pull-in instability. Proc. Natl. Acad. Sci. 107 (10), 4505–4510.

Kim, K.J., Tadokoro, S., 2007. Electroactive polymers for robotic applications. In: Artificial Muscles and Sensors. Springer, New York, p. 291.

Li, J.R., Liu, L.W., Liu, Y.J., Leng, J.S., 2014. Dielectric elastomer bending actuator: experiment and theoretical analysis. In: Electroactive Polymer Actuators and Devices (EAPAD) 2014, 9056. Int. Soc. Opt. Photo., p. 905639.

Li, T.F., Keplinger, C., Baumgartner, R., Bauer, S., Yang, W., Suo, Z.G., 2013. Giant voltage-induced deformation in dielectric elastomers near the verge of snap-through instability. J. Mech. Phys. Solids 61 (2), 611–628.

Li, T.F., Li, G.R., Liang, Y.M., Cheng, T.Y., Dai, J., Yang, X.X., Liu, B.Y., Zeng, Z.D., Huang, Z.L., Luo, Y.W., Xie, T., Yang, W., 2017. Fast-moving soft electronic fish. Sci. Adv. 3 (4), E1602045.

Liu, L.P., 2013. On energy formulations of electrostatics for continuum media. J. Mech. Phys. Solids 61 (4), 968–990.

Liu, X.J., Li, B., Chen, H.L., Jia, S.H., Zhou, J.X., 2016. Voltage-induced wrinkling behavior of dielectric elastomer. J. Appl. Polym. Sci. 133, 1–8.

Ogden, R.W., 1997. Non-Linear Elastic Deformations. Dover, New York.

O'Halloran, A., O'Malley, F., McHugh, P., 2008. A review on dielectric elastomer actuators, technology, applications, and challenges. J. Appl. Phys. 104 (7), 9.

Pelrine, R., Kornbluh, R., Pei, Q.B., Joseph, J., 2000. High-speed electrically actuated elastomers with strain greater than 100%. Science 287 (5454), 836–839.

Plante, J.S., Dubowsky, S., 2006. Large-scale failure modes of dielectric elastomer actuators. Int. J. Solids Struct. 43, 7727–7751.

Rasmussen, L. (Ed.), 2012. Electroactivity in Polymeric Materials.. Springer Science & Business Media.

Rivlin, R.S., 1949. Large elastic deformations of isotropic materials. v. the problem of flexure. Proc. R. Soc. A 195, 463–473.

Roccabianca, S., Gei, M., Bigoni, D., 2010. Plane strain bifurcations of elastic layered structures subject to finite bending: theory versus experiments. IMA J. Appl. Math. 75 (4), 525–548.

Shmuel, G., deBotton, G., 2013. Axisymmetric wave propagation in finitely deformed dielectric elastomer tubes. Proc. Roy. Soc. A 469, 20130071.

Sigaeva, T., Mangan, R., Vergori, L., Destrade, M., Sudak, L., 2018. Wrinkles and creases in the bending, unbending and eversion of soft sectors. Proc. R. Soc. A 474, 20170827.

Su, Y.P., Wang, H.M., Zhang, C.L., Chen, W.Q., 2016a. Propagation of non-axisymmetric waves in an infinite soft electroactive hollow cylinder under uniform biasing fields. Int. J. Solids Struct. 81, 262–273.

Su, Y.P., Zhou, W.J., Chen, W.Q., Lú, C.F., 2016b. On buckling of a soft incompressible electroactive hollow cylinder. Int. J. Solids Struct. 97, 400–416.

Sun, J.Y., Keplinger, C., Whitesides, G.M., Suo, Z.G., 2014. Ionic skin. Adv. Mater. 26 (45), 7608–7614.

Suo, Z.G., Zhao, X.H., Greene, W.H., 2008. A nonlinear field theory of deformable dielectrics. J. Mech. Phys. Solids 56 (2), 467–486.

Toupin, R.A., 1956. The elastic dielectric. J. Ration. Mech. Anal. 5 (6), 849–915.

Triantafyllidis, N., 1980. Bifurcation phenomena in pure bending. J. Mech. Phys. Solids 28 (3–4), 221–245.

Truesdell, C., Toupin, R., 1960. The classical field theories. In: Principles of Classical Mechanics and Field Theory/Prinzipien der Klassischen Mechanik und Feldtheorie. Springer, Berlin, Heidelberg, pp. 226–858.

Wang, Q.M., Zhao, X.H., 2013. Creasing-wrinkling transition in elastomer films under electric fields. Phys. Rev. E. 88, 042403.

Wissman, J., Finkenauer, L., Deseri, L., Majidi, C., 2014. Saddle-like deformation in a dielectric elastomer actuator embedded with liquid-phase gallium-indium electrodes. J. Appl. Phys. 116 (14), 144905.

Wu, B., Su, Y.P., Chen, W.Q., Zhang, C.Z., 2017. On guided circumferential waves in soft electroactive tubes under radially inhomogeneous biasing fields. J. Mech. Phys. Solids 99, 116–145.

Wu, B., Zhou, W.J., Bao, R.H., Chen, W.Q., 2018. Tuning elastic waves in soft phononic crystal cylinders via large deformation and electromechanical coupling. J. Appl. Mech. 85 (3), 031004.

Zhang, H., Wang, Y.X., Godaba, H., Khoo, B.C., Zhang, Z.S., Zhu, J., 2017. Harnessing dielectric breakdown of dielectric elastomer to achieve large actuation. J. Appl. Mech. 84 (12), 121011.

Zhu, J., Stoyanov, H., Kofod, G., Suo, Z.G., 2010. Large deformation and electromechanical instability of a dielectric elastomer tube actuator. J. Appl. Phys. 108 (7), 074113.